

Galaxy Rotation Curves Without Non-Baryonic Dark Matter

J. R. Brownstein¹ and J. W. Moffat²

The Perimeter Institute for Theoretical Physics, Waterloo, Ontario, N2J 2W9, Canada

and

Department of Physics, University of Waterloo, Waterloo, Ontario N2Y 2L5, Canada

ABSTRACT

We apply the modified acceleration law obtained from Einstein gravity coupled to a massive skew symmetric field $F_{\mu\nu\lambda}$ to the problem of explaining galaxy rotation curves without exotic dark matter. Our sample of galaxies includes low surface brightness (LSB) and high surface brightness (HSB) galaxies, and an elliptical galaxy. In those cases where photometric data are available, a best fit via the single parameter $(M/L)_{\text{stars}}$ to the luminosity of the gaseous (HI plus He) and luminous stellar disks is obtained. Additionally, a best fit to the rotation curves of galaxies is obtained in terms of a parametric mass distribution (independent of luminosity observations) – a two parameter fit to the total galactic mass, (or mass-to-light ratio M/L), and a core radius associated with a model of the galaxy cores using a nonlinear least-squares fitting routine including estimated errors. The fits are compared to those obtained using Milgrom’s phenomenological MOND model and to the predictions of the Newtonian-Kepler acceleration law.

Subject headings: dark matter — galaxies: general — galaxies: kinematics and dynamics — galaxies: fundamental parameters

1. Introduction

In spite of intensive searches for the components of non-baryonic dark matter, no candidate particles have been observed. This leads one to search for a gravity theory that can

¹jbrownstein@perimeterinstitute.ca

²john.moffat@utoronto.ca

explain galaxy dynamics without the need for exotic dark matter. Such a possible model was introduced in [Milgrom \(1983\)](#), and for more than twenty years since its publication, attempts to form a consistent relativistic theory containing Milgrom’s phenomenological model have been pursued ([Bekenstein 2004](#); [Sanders 2005](#)). A generalization of Einstein’s general relativity (GR) based on a pseudo-Riemannian metric tensor and a skew symmetric rank three tensor field $F_{\mu\nu\lambda}$, called metric-skew-tensor-gravity (MSTG), leads to a modified acceleration law that can explain the flat rotation curves of galaxies and cluster lensing without postulating exotic dark matter ([Moffat 2005a](#)). A relativistic scalar-tensor-vector gravity (STVG) theory has also been developed which yields the same modified acceleration law as MSTG, and provides an effective description of the running of the G , γ_c and μ with space and time ([Moffat 2005b](#)).

A cosmological model obtained from the field equations and a running of the effective gravitational coupling constant G can also explain the growth of large scale structure formation without invoking cold dark matter. The running of the cosmological constant would produce a quintessence-like dark energy that could account for the acceleration of the expansion of the universe ([Perlmutter *et al.* 1997](#); [Riess *et al.* 1998, 2004](#); [Garnavich *et al.* 1998](#); [Spergel *et al.* 2003](#); [Bennett *et al.* 2003](#)).

A renormalization group (RG) framework ([Reuter & Weyer 2004a,b](#)) for MSTG was developed to describe the running of the effective gravitational coupling constant G , and the effective coupling constant γ_c that measures the strength of the coupling of the $F_{\mu\nu\lambda}$ field to matter. A momentum cutoff identification $k = k(x)$ associates the RG scales to points in spacetime. For the static, spherically symmetric solution, the RG flow equations allow a running with momentum k and proper length $\ell(r) = 1/k$ and provides for a spatial variation of the effective Newton’s coupling constant, $G = G(r)$; together with a variation of the skew field coupling constant, $\gamma_c(r)$, to matter; and the effective mass of the skew field $\mu = \mu(r) = 1/r_0$ where r denotes the radial coordinate. Such a “running” of coupling constants and mass are well-known from particle physics (e.g. quantum chromodynamics) and condensed matter and are applied here to the behavior of the infrared fixed point of the renormalization group method of quantum gravity. The form of $G(r)$ as a function of r , obtained from the modified Newtonian acceleration law, leads to agreement with solar system observations, terrestrial gravitational experiments and the binary pulsar PSR 1913+16 observations, while strong renormalization effects in the infrared regime at large distances lead to fits to galaxy rotation curves.

In this paper, a fit to both low surface brightness (LSB) and high surface brightness (HSB) galaxies over the range from dwarf galaxies to giant galaxies is achieved in terms of the total galaxy mass M (or M/L) without exotic dark matter. A satisfactory fit is achieved

to the rotational velocity data generic to the elliptical galaxy NGC 3379. A model of the modified acceleration law that includes a description of radial velocity curves in the core of galaxies as well as in the outer regions of the galaxy is shown to yield good fits to rotational velocity data. The significance of this result is made explicit by the depth of the galaxy rotation curve study, here. We performed photometric fits to 58 HSB and LSB and Dwarf galaxies utilizing a single parameter – the M/L ratio of the stellar disk. 29 of these galaxies were based upon B -band and the remaining 29 galaxies were based upon K -band. The K -band data is the more modern data set and is a more precise tracer of the mean radial distribution of the dominant stellar population – these were the photometric results of Ursa Major. Since 2001, the Ursa Major data has been revised since the estimated distance to the cluster is now taken as 18.6 Mpc as opposed to the original publication’s use of 15.5 Mpc. We updated the original analysis of Sanders & Verheijen (1998) using that group’s Groningen Image Processing System (GIPSY)¹.

In addition, we performed 101 galaxy rotation curve fits to HSB and LSB and Dwarf galaxies (including the 58 galaxies that were fit photometrically) using a parametric mass distribution. These fits were necessary for those galaxies for which photometric data of the HI gas (corrected for He component) and stellar disk was unavailable. Although the model contains two parameters as opposed to one parameter for the photometric fits, it makes no assumptions on the constancy of the M/L ratio within a galaxy although it does not distinguish between gas or stellar disk.

A comparison of the fits to the rotational velocity curve data obtained from MSTG and Milgrom’s MOND reveals that the results from both models are qualitatively similar for almost all of the galaxy data fitted, although predictions of the galactic masses differ.

2. Modified Acceleration Law

From the derivation of the radial acceleration experienced by a test particle in a static, spherically symmetric gravitational field due to a point source, we obtain (Moffat 2005a,b):

$$a(r) = -\frac{G_\infty M}{r^2} + \sigma \frac{\exp(-r/r_0)}{r^2} \left(1 + \frac{r}{r_0}\right). \quad (1)$$

Here, G_∞ is defined to be the *effective* gravitational constant at infinity

$$G_\infty = G_0 \left(1 + \sqrt{\frac{M_0}{M}}\right), \quad (2)$$

¹<http://www.astro.rug.nl/~gipsy/>

where G_0 is Newton’s “bare” gravitational constant. This conforms with our definition of G in the RG flow formalism, which requires that the effective G be renormalized in order to guarantee that equation (1) reduces to the Newtonian acceleration

$$a_{\text{Newton}} = -\frac{G_0 M}{r^2} \quad (3)$$

at small distances $r \ll r_0$. We model the coupling constant σ for the repulsive Yukawa force contribution in equation (1) by

$$\sigma = G_0 \sqrt{M_0 M}, \quad (4)$$

where M_0 is a coupling parameter. We obtain the acceleration on a point particle

$$a(r) = -\frac{G_\infty M}{r^2} + G_0 \sqrt{M M_0} \frac{\exp(-r/r_0)}{r^2} \left(1 + \frac{r}{r_0}\right). \quad (5)$$

By using equation (2), we can express the modified acceleration in the form

$$a(r) = -\frac{G_0 M}{r^2} \left\{ 1 + \sqrt{\frac{M_0}{M}} \left[1 - \exp(-r/r_0) \left(1 + \frac{r}{r_0}\right) \right] \right\}. \quad (6)$$

We can rewrite equation (6) as

$$a(r) = -\frac{G(r)M}{r^2}, \quad (7)$$

where

$$G(r) = G_0 \left\{ 1 + \sqrt{\frac{M_0}{M}} \left[1 - \exp(-r/r_0) \left(1 + \frac{r}{r_0}\right) \right] \right\}. \quad (8)$$

Thus, $G(r)$ describes the running with distance of the effective gravitational constant in the RG flow scenario.

The gravitational potential for a point source obtained from the modified acceleration formula (6) is given by

$$\Phi(r) = \frac{G_0 M}{r} \left[1 + \sqrt{\frac{M_0}{M}} (1 - \exp(-r/r_0)) \right]. \quad (9)$$

We apply equation (6) to explain the flatness of rotation curves of galaxies, as well as the approximate Tully-Fisher law (Tully & Fisher 1977), $v^4 \propto G_0 M \propto L$, where v is the rotational velocity of a galaxy, M is the galaxy mass

$$M = M_{\text{stars}} + M_{\text{HI}} + M_{\text{DB}} + M_f, \quad (10)$$

and L is the galaxy luminosity. Here, M_{stars} , M_{HI} , M_{DB} and M_f denote the visible mass, the mass of neutral hydrogen, possible dark baryon mass and gas, and the mass from the skew field energy density, respectively.

The rotational velocity of a star v obtained from $v^2(r)/r = a(r)$ is given by

$$v(r) = \sqrt{\frac{G_0 M}{r}} \left\{ 1 + \sqrt{\frac{M_0}{M}} \left[1 - \exp(-r/r_0) \left(1 + \frac{r}{r_0} \right) \right] \right\}^{1/2}. \quad (11)$$

Let us postulate that the parameters M_0 and r_0 give the magnitude of the constant acceleration

$$a_0 = \frac{G_0 M_0}{r_0^2}. \quad (12)$$

We assume that for galaxies and clusters of galaxies this acceleration is determined by

$$a_0 = cH_0. \quad (13)$$

Here, H_0 is the current measured Hubble constant $H_0 = 100 h \text{ km s}^{-1} \text{ Mpc}^{-1}$ where $h = (0.71 \pm 0.07)$ (Eidelman *et al.* 2004)². This gives

$$a_0 = 6.90 \times 10^{-8} \text{ cm s}^{-2}. \quad (14)$$

We note that $a_0 = cH_0 \sim (\sqrt{\Lambda/3})c^2$, so there is an interesting connection between the parameters M_0 , r_0 and the cosmological constant Λ .

Let us now describe a model of a spherically symmetric galaxy such that the density of visible matter, $\rho(r)$, contains an inner core at radius $r = r_c$. The acceleration law of equation (6) takes the form

$$a(r) = -\frac{G_0 \mathcal{M}(r)}{r^2} \left\{ 1 + \sqrt{\frac{M_0}{M}} \left[1 - \exp(-r/r_0) \left(1 + \frac{r}{r_0} \right) \right] \right\}, \quad (15)$$

where

$$\mathcal{M}(r) = 4\pi \int_0^r dr' r'^2 \rho(r') \quad (16)$$

is the total amount of ordinary matter within a sphere of radius r . A simple model for $\mathcal{M}(r)$ is

$$\mathcal{M}(r) = M \left(\frac{r}{r_c + r} \right)^{3\beta}, \quad (17)$$

²<http://pdg.lbl.gov>

where

$$\beta = \begin{cases} 1 & \text{for HSB galaxies,} \\ 2 & \text{for LSB \& Dwarf galaxies.} \end{cases} \quad (18)$$

The constituents of M in equation (15) and (17) are determined by equation (10). The density of ordinary matter is given by

$$\frac{d\mathcal{M}(r)}{dr} = 4\pi r^2 \rho(r) \equiv 3\beta \mathcal{M}(r) \left[\frac{r_c}{r(r+r_c)} \right], \quad (19)$$

so that we have

$$\rho(r) = \frac{3}{4\pi r^3} \beta \mathcal{M}(r) \left[\frac{r_c}{r+r_c} \right]. \quad (20)$$

Well inside the core radius, where $r \ll r_c$, the density $\rho(r) \propto \text{constant}$ for HSB galaxies with $\beta = 1$. Although for LSB galaxies, it is the case for $\beta = 2$ that $\rho(r) \propto (r/r_c)^3$ for $r \ll r_c$. This behavior is quickly suppressed and the density profile shows no rapid change for $r \ll r_c$. Indeed the choice of $\beta = 2$ for LSB galaxies was found to be favorable because it resulted in a more slowly rising mass profile (the integrated density distribution) for small r . This critical distinction between high and low surface brightness galaxies has been studied in the context of cold dark matter, with the common conclusion that the rotation curves of LSB and Dwarf galaxies rise more slowly than those of HSB galaxies (or elliptical galaxies) (de Blok & McGaugh 1996; de Blok *et al.* 2003; Bailin *et al.* 2005). However, the ordinary matter density of equation (20) does not exhibit the divergent or cuspy behavior for either HSB or LSB galaxies, contrary to the observations in these cold dark matter studies. Moreover, provided $r_c \ll r_0$ (which is the result for all the galaxies fitted), then we see that the exponential factor in the acceleration law of equation (15) has a damping effect well within the core radius such that the dynamics for $r \ll r_c$ is described by Newtonian theory. Thus the high resolution rotation curves for the LSB galaxies provide a clean testing ground for any theory of galaxy rotation curves. Without the distinction we have implemented by equation (18), the quality of our rotation curve fits would not be as good.

Well outside the core radius, where $r \gg r_c$, equation (17) implies that

$$\lim_{r \gg r_c} \mathcal{M}(r) = M, \quad (21)$$

and the acceleration is described by equation (6).

For those galaxies for which there is photometric data available, the observed luminosity of the gaseous disk (HI plus He), and the stellar components (the disk and separately the bulge) can be used to provide a more precise fit to the velocity curve data, which would include the kinkiness of the rotation curves. By assuming a constant M/L ratio, it is possible to invert the Poisson equation for the potential, yielding the mass distributions of the

individual constituents. This results in a single parameter fit – $(M/L)_{\text{stars}}$. By including the bulge, a more precise fit is possible, in principle. However this would necessitate a second parameter $(M/L)_{\text{bulge}}$ which may be seen as a weakness to this approach. We choose to provide the single parameter fit – which we present for comparison. We note that the assumption of constant ratio M/L forces an averaging over the radial distances thereby working to reduce the accuracy of the photometric fits. Our parametric mass model requires no assumptions on the ratio of M/L . The photometric fits also include the assumption that the HI gas is on stable circular orbits around the centers of the galaxies. This assumption may be violated for interacting galaxies, or in galaxies with strong bars. The photometric fits also utilize a correction of the mass for the Helium fraction, which is based on the results from Big-Bang nucleosynthesis and is not well known.

The rotational velocity derived from the acceleration law equation (15) is

$$v(r) = \sqrt{\frac{G_0 M}{r}} \left(\frac{r}{r_c + r} \right)^{\frac{3}{2}\beta} \left\{ 1 + \sqrt{\frac{M_0}{M}} \left[1 - \exp(-r/r_0) \left(1 + \frac{r}{r_0} \right) \right] \right\}^{1/2}. \quad (22)$$

The modified acceleration law equation (15) can be compared to the Newtonian law using equation (17):

$$a_{\text{Newton}}(r) = -\frac{G_0 \mathcal{M}(r)}{r^2}. \quad (23)$$

The gravitational acceleration described by Milgrom’s phenomenological MOND model (Milgrom 1983; Sanders & McGaugh 2002) is given by

$$a \mu \left(\frac{a}{a_{0\text{Milgrom}}} \right) = a_{\text{Newton}}, \quad (24)$$

where $\mu(x)$ is a function that interpolates between the Newtonian regime, $\mu(x) = 1$, when $x \gg 1$ and the MOND regime, $\mu(x) = x$, when $x \ll 1$. The function normally used for galaxy fitting is

$$\mu(x) = \frac{x}{\sqrt{1 + x^2}}. \quad (25)$$

3. Galaxy Rotational Velocity Curves

A good fit to LSB and HSB galaxy data is obtained with the parameters

$$M_0 = 9.60 \times 10^{11} M_{\odot}, \quad r_0 = 13.92 \text{ kpc} = 4.30 \times 10^{22} \text{ cm}, \quad (26)$$

where we have substituted the value of a_0 from equation (14) into equation (12), relating the parameters M_0 and r_0 . Thus, the modified acceleration law contains only a single parameter,

M_0 or r_0 , which once set as in equation (26) is universal for galaxies and is no longer a free parameter for fitting the galaxy rotation curves.

We allow for the smaller scale Dwarf galaxies, for which the outermost observed radial position, $r_{\text{out}} \lesssim 12$ kpc, by rescaling equation (26) such that the values for M_0 and r_0 continue to satisfy the conditions (12) and (13):

$$M_0 = 2.40 \times 10^{11} M_{\odot}, \quad r_0 = 6.96 \text{ kpc} = 2.15 \times 10^{22} \text{ cm}. \quad (27)$$

The RG flow equations do indeed require that the parameters M_0 and r_0 are scale parameters and thus it is expected that while we may obtain reasonable fits assuming they are roughly constant within a set population, this is an approximation. We are able to fit all HSB galaxies with a fixed M_0 and r_0 . We are also able to fit all LSB and Dwarf galaxies by rescaling the HSB fixed values of M_0 and r_0 by a factor of 4 and 2, respectively. This is done to keep the number of parameters to an absolute minimum while respecting the fact that the parameters r_0 and M_0 are determined by the scale of the system and should be different for HSB vs. LSB and Dwarf galaxies.

The fits to the galaxy rotation curves, v , in km/s versus the galaxy radius, r , in kpc are shown in Figs. 1 through 5. The acceleration law is given by equation (15); and the rotational velocity by equation (22).

3.1. Photometric Velocity Curve Fits

The fits to the data in Fig. 1 and 5 are based on the photometric data of the gaseous disk (HI plus He) component and luminous stellar disk component and only a single parameter $(M/L)_{\text{stars}}$ is used to fit the rotation curves. The data includes 29 galaxies – both LSB and HSB galaxies – obtained from de Blok & McGaugh (1998); de Blok *et al.* (2001a,b); Begeman *et al.* (1991); McGaugh *et al.* (2001); Sanders & McGaugh (2002); Sanders (1996) and an additional 29 galaxies from the Ursa Major (UMa) cluster of galaxies derived from Sanders & Verheijen (1998); Verheijen (2001); Verheijen & Sancisi (2001). For the UMa cluster of galaxies, available K -band data was used to reproduce the velocity profiles of the gaseous disk (HI plus He) distribution and luminous stellar disks (via the ROTMOD task of GIPSY³). The gaseous disk (HI plus He) was assumed to be infinitely thin and to have a total mass given by

$$M_{\text{gas}} = \frac{4}{3} M_{\text{HI}} \quad (28)$$

³<http://www.astro.rug.nl/~gipsy/>

where the He correction factor of 4/3 is roughly determined from Big Bang nucleosynthesis, and the value of

$$M_{HI} = 2.36 \times 10^5 D^2 \int Sdv [M_{\odot}], \quad (29)$$

where $\int Sdv$ is the integrated HI flux density in units of Jy km/s as measured from the global HI profile – taken from Column (15) of Table 2 of Verheijen (2001), and D is the distance in Mpc. We accounted for the revised distance estimate to UMa from $D = 15.5$ Mpc to $D = 18.6$ Mpc which has changed since the rotation curves were originally presented in Sanders & Verheijen (1998). The luminous stellar disk was assumed to be described by the Van der Kruit and Searle law, where the disk density distribution as a function of z (vertical height from the plane of the disk) is given by

$$\Sigma(z) = \text{sech}^2(z/z_0)/z_0, \quad (30)$$

where z_0 is the vertical scale height of the luminous stellar disk, and was assumed to be 20% of the near infrared exponential disk scale length according to Column (13) of Table 2 of Verheijen (2001).

According to Sanders & Verheijen (1998) the existence of K -band surface photometry is a great advantage since the near-infrared emission, being relatively free of the effects of dust absorption and less sensitive to recent star formation, is a more precise tracer of the mean radial distribution of the dominant stellar population. The principal advantages of using infrared luminosities is that stellar mass-to-light ratios are less affected by population differences and extinction corrections are minimal (Verheijen 2001). We focus on NGC 4010 in Fig. 5 to study the effect of the extended HI and K -band data (beyond the rotation curve data) on the quality fits in MSTG and MOND. The numerical results of the UMa fits are presented in Table 2.

3.2. Parametric Velocity Curve Fits

The fits to the rotation curve data shown in Figs. 2 through 4 are based on the parametric model of equations (17) and (18). Since this model is independent of the photometric data of the gaseous disk (HI plus He) component and luminous stellar disk component, a larger database of galaxies is available including the high resolution rotation curves of Sofue (1996) and the elliptical galaxy NGC 3379 of Romanowsky *et al.* (2003, 2004). This adds another 42 galaxies to the *complete sample* as described in Table 1. We focus on the Milky Way in Fig. 3 and NGC 3379 in Fig. 4 to clarify the predictions of MOND and MSTG which are hard to distinguish in Fig. 2; but become apparent at distances beyond the edge of the visible stars. The numerical results of the fits to the *complete sample* are presented in Table 3.

3.3. Flat Rotation Velocity

In Milgrom’s phenomenological MOND model we have

$$v_c^4 = G_0 M a_{0\text{Milgrom}}. \quad (31)$$

We see that equation (31) predicts that the rotational velocity is constant out to an infinite range and the rotational velocity does not depend on a distance scale, but on the magnitude of the acceleration $a_{0\text{Milgrom}}$. In contrast, our modified acceleration formula does depend on the radius r and the distance scale r_0 , which for galaxies is fixed by the formula equation (13). The MSTG velocity curve asymptotically becomes the same as the Newtonian-Kepler prediction as $r \rightarrow \infty$:

$$v \sim \sqrt{G_\infty M/r}, \quad (32)$$

where G_∞ is the renormalized value of Newton’s constant.

The flatness of the rotation curves arises due to an increased strength in the galactic gravitational potential due to the running of Newton’s constant. By taking the first and second derivative of $G(r)$ from equation (8):

$$\frac{dG(r)}{dr} = \frac{G_0}{r_0^2} \sqrt{\frac{M_0}{M}} r \exp(-r/r_0), \quad (33)$$

$$\frac{d^2G(r)}{dr^2} = \frac{G_0}{r_0^2} \sqrt{\frac{M_0}{M}} \left(1 - \frac{r}{r_0}\right) \exp(-r/r_0), \quad (34)$$

and we see that $dG(r)/dr$ has a maximum at $r = r_0$. Therefore the rate of change of the running of the effective gravitational constant has a maximum; and it is at this point where the tendency to return to the Newtonian-Kepler behaviour of equation (32) is most opposed by the RG flow. The effect of this on the galaxy rotation curves is to produce an extended region where the curve seems flat. The velocity at $r = r_0$ is defined as v_0 :

$$v_0 \equiv v(r = r_0), \quad (35)$$

is the MSTG equivalent of the flat rotational velocity; and is within the quoted experimental uncertainties to the MOND equivalent, v_c , in those galaxies that MOND handles well. The numerical results for v_0 and v_c with calculated uncertainties are included in Tables 2 and 3.

Using the Sloan Digital Sky Survey (SDSS), Prada *et al.* (2003) have studied the velocities of satellites orbiting isolated galaxies. They detected approximately 3000 satellites, and they found that the line-of-sight velocity dispersion of satellites declines with distance to the primary. The velocity was observed to decline to a distance of ~ 350 kpc for the available data. This result contradicts the constant velocity prediction equation (31) of MOND, but

is consistent with the MSTG prediction equation (32). It also agrees with the cosmological models which predict mass profiles of dark matter halos at large distances. During the last two decades of numerical modelling of galaxy formation, they have produced a density profile of dark matter halos, $\rho \propto 1/r^3$ at large radii, which does not depend on the nature of the dark matter (Avila-Reese *et al.* 2001; Colin *et al.* 2002). The results of Prada *et al.* (2003) are consistent with recent gravitational lensing results (Sheldon *et al.* 2003).

4. The Tully-Fisher Relation

Unlike MOND, the mass – rotational velocity relationship is not absolute as in equation (31); and indeed at distances beyond the galaxy it is expected that Kepler’s Law applies according to equation (32).

The observational Tully-Fisher relation implies a luminosity – rotational velocity of the form (Tully & Fisher 1977):

$$L \propto v_{\text{out}}^a \text{ where } a \approx 4, \quad (36)$$

where L is the total observed luminosity of the galaxy (in units of $10^{10}L_{\odot}$), and v_{out} is the observed velocity at the outermost observed radial position (in km/s). Verheijen (2001) considers an alternate definition of the “flat rotation velocity”, v_{flat} , which categorizes galaxies according to three kinds depending on the shape of the rotation curve. The behavior of v_{out} is more closely related to the asymptotic “flat rotation velocity”. Taking the logarithm of both sides of equation (36), we obtain

$$\log(L) = a \log(v_{\text{out}}) + b. \quad (37)$$

B -band luminosity data is available for practically all of the galaxies either from the original references listed in Table 3 or listed in Tully (1988). Moreover, the majority of the galaxies in this study have been detected by 2MASS in the K_s -band. In order to calculate the total K -band luminosity, apparent K -band magnitudes from the 2MASS survey were used. Given an apparent K -band magnitude it is possible to calculate the K -band luminosity as

$$\log_{10}(L_K) = 1.364 - \frac{2}{5}K_T + \log_{10}(1 + z) + 2 \log_{10} D, \quad (38)$$

where L_K is the K -band luminosity in units of $10^{10}L_{\odot}$, K_T is the K -band apparent magnitude and z is the redshift of the galaxy (determined from the NASA/IPAC Extragalactic Database), and D is the distance to the galaxy in Mpc (from the original references). The $\log_{10}(1 + z)$ term is a first order K -correction. We have plotted the observed Tully-Fisher relation for LSB and HSB galaxies in Fig. 6.

As in (Sanders & Verheijen 1998), MOND is able to make predictions on both the slope and the intercept of the logarithmic Tully-Fisher relation by assuming that the mass to luminosity ratio, M/L , is constant across all galaxies. Although this is not the case, the assumption is enforced by using the mean mass to light ratio, $\langle M/L \rangle$, to determine the values of the slope and intercept, a and b , in equation (37). Replacing the observed luminosity, L , in the logarithmic Tully-Fisher relation of equation (37) with

$$L = \frac{M}{\langle M/L \rangle}. \quad (39)$$

We obtain

$$\log(M) = a \log(v_{\text{out}}) + b - \log(\langle M/L \rangle). \quad (40)$$

Thus, the effect of $\langle M/L \rangle$ is to shift the intercept which vanishes when $\langle M/L \rangle = 1$. We may quantify the predictions of MSTG and MOND by either computing the appropriate $\langle M/L \rangle$ values which depend on the particular band of the luminosity measurements, or by considering the respective curve fits to the actual Tully-Fisher relation:

$$\log(M) = a \log(v_0) + b \quad \text{MSTG} \quad (41)$$

$$\log(M) = a \log(v_c) + b \quad \text{MOND} \quad (42)$$

where v_0 is the MSTG “flat rotation velocity” of equation (35); and v_c is the MOND asymptotic rotation velocity of equation (31). Taking the logarithm (with respect to base 10) of both sides of equation (31), we have the MOND predictions

$$a = 4, \quad (43)$$

$$b = -8.21 \quad (44)$$

Fig. 7 shows the curve fits to equations (41) and (42) for both the photometric fits and the fits to our parametric model of equations (17) and (18). In all cases, we are able to combine the HSB, LSB and Dwarf galaxy data (and the elliptical galaxy NGC 3379) for the fitting, implying consistent physics across galaxies. The numerical results of the respective fits are presented in Table 4.

We see that a comparison of the MSTG and MOND results of the actual and observed Tully-Fisher relation show that the MSTG prediction is closer to the observational data for the *complete sample* and the UMa B -band photometry. This is most likely the result of the implicit assumption within the MOND framework that M/L is constant within each galaxy which does not appear to be the case in either the B - or K - bands.

5. Conclusions

A gravity theory consisting of a metric-skew-tensor action that leads to a modified Newtonian acceleration law (Moffat 2005a,b) can be fitted to a large class of galaxy rotation curves. We have presented the predictions for the galaxy rotation curves from a covariant and relativistic gravitational theory without postulating non-baryonic dark matter. The only other relativistic gravity theories that have been published that have attempted to do this are Mannheim (1990, 2005) and Bekenstein (2004). The latter recent publication attempts to incorporate Milgrom’s MOND into a covariant gravitational theory. The fully relativistic gravitational theory presented in Moffat (2005a,b) is a consistent and viable example of a gravitational theory that fits the galaxy rotation curves and galaxy cluster mass X-ray data without non-baryonic dark matter Brownstein & Moffat (2005). The large sample of galaxy data which fits our predicted MSTG acceleration law warrants taking seriously the proposal that a modified gravity theory can explain the flat rotational velocity curves of galaxies without (as yet, undetected) non-baryonic dark matter. It represents an important foil in comparing modified gravitational theory with dark matter.

It is interesting to note that we can fit the rotational velocity data of galaxies in the distance range $0.02 \text{ kpc} < r < 70 \text{ kpc}$ and in the mass range $10^5 M_\odot < M < 10^{11} M_\odot$ without exotic dark matter halos. The lensing of clusters can also be explained by the theory without exotic dark matter in cluster halos. An important prediction is that for large enough distances from the galaxy cores, the rotational velocity of stars declines as $v \propto 1/\sqrt{r}$ consistent with a Newtonian-Kepler fall off. This is consistent with the results of Prada *et al.* (2003) and gravitational lensing results for galaxies clusters (Sheldon *et al.* 2003).

In order to obtain a self-consistent description of solar dynamics, galaxies, clusters of galaxies and cosmology, it is necessary to have the effective gravitational constant G , the MSTG coupling constant γ_c , the mass μ (range r_0) of the skew field $F_{\mu\nu\lambda}$ and the cosmological constant Λ run with distance (time). The RG flow effective action description of MSTG quantum gravity allows for a running of these effective constants with distance and time (Moffat 2005a,b). The RG flow framework for the theory is characterized by special RG trajectories. On the RG trajectory, we identify a regime of distance scales where solar system gravitational physics is well described by GR, which is contained in MSTG as an approximate solution to the field equations. We are able to obtain agreement with the observations in the solar system, terrestrial gravitational experiments and the binary pulsar PSR 1913+16. Strong infrared renormalization effects become visible at the scale of galaxies and the modified Newtonian potential replaces exotic dark matter as an explanation of flat rotation curves. Thus, gravity becomes a “confining force” that has significant predictions for astrophysics and cosmology.

We have demonstrated that the RG flow running of G and MSTG cosmology can lead to a description of the universe that does not require dominant, exotic dark matter. Dark energy is described by an effective time dependent cosmological constant. A detailed investigation of the MSTG cosmological scenario must be performed to establish that it can describe the large scale structure of the universe, account for galaxy formation and big bang nucleosynthesis and be consistent with the WMAP data.

The predictions for the galaxy rotation curves from MSTG and Milgrom’s MOND agree remarkably for almost all of the 101 galaxies fitted throughout the visible distance scales of the galaxies for LSBs as well as HSBs and the one elliptical galaxy NGC 3379. In particular, for the fits using photometric data and only one parameter $\langle M/L \rangle$ (once r_0 and M_0 are fixed), the agreement of the two models suggests that Milgrom’s MOND critical acceleration $a_{0\text{Milgrom}} = 1.2 \times 10^{-8} \text{ cm/s}^2$ is closely related to the range parameter r_0 and the distance scaling behavior of the MSTG modified acceleration law.

Acknowledgments

This work was supported by the Natural Sciences and Engineering Research Council of Canada. JRB would like to thank the Perimeter Institute for Theoretical Physics for additional funding. We thank Martin Green and Martin Reuter for helpful discussions. We also thank Stacy McGaugh and Marc Verheijen for supplying data and for helpful discussions; and Erwin de Blok for assisting in our deployment of the Groningen Image Processing System (GIPSY)⁴ and the ROTMOD task on the Mac G4 platform.

REFERENCES

- Avila-Rees, V., Colin, P., Valenzuela, O., D’Onghia, E. & Firmani, C. 2001, ApJ, 559, 516 ([astro-ph/0010525](#))
- Bailin, J., Power, C., Gibson, B.K. & Steinmetz M. 2005, MNRAS, submitted ([astro-ph/0502231](#))
- Bekenstein, J.D. 2004, Phys. Rev. D70, 083509 ([astro-ph/0403694](#))
- Begeman, K.G., Broeils, A.H. & Sanders, R.H. 1991 MNRAS, 249, 523 ([1991MNRAS.249..523B](#))

⁴<http://www.astro.rug.nl/~gipsy/>

- Bennett, C.L. *et al.* 2003, ApJS, 148, 1 ([astro-ph/0302207](#))
- Brownstein, J.R. & Moffat, J.W. 2005, preprint ([astro-ph/0507222](#))
- Colin, P., Avila-Rees, V., Valenzuela, O. & Firmani, C. 2002, ApJ, 581, 777 ([astro-ph/0205322](#))
- de Blok, W. J. G. & McGaugh, S.S. 1996, ApJ, 469, 89 ([astro-ph/9607042](#))
- de Blok, W. J. G. & McGaugh, S.S. 1998, ApJ, 508, 132 ([astro-ph/9805120](#))
- de Blok, W.J.G., McGaugh, S.S., Bosma, A. & Rubin, V.C. 2001, ApJ, 552, L23 ([astro-ph/0103102](#))
- de Blok, W. J. G., McGaugh, S.S. & Rubin, V.C. 2001, AJ, 122, 2396 ([astro-ph/0107366](#))
- de Blok, W. J. G., Bosma, A. & McGaugh, S.S. 2003, MNRAS, 340, 657 ([astro-ph/0212102](#))
- Eidelman, S. *et al.* 2004, Phys. Lett. B592, 1
- Garnavich, P.M. *et al.* 1998, ApJ, 509, 74 ([astro-ph/9806396](#))
- McGaugh, A., Rubin, V.C. & de Blok, W. J. G. 2001, AJ, 122, 2381 ([astro-ph/0107326](#))
- Mannheim, P.D. 2005, preprint ([astro-ph/0505266](#))
- Mannheim, P.D. 1990, Gen. Rel. Grav., 22, 289
- Milgrom, M. 1983, ApJ, 270, 365
- Moffat, J.W. 2005, J. Cosmology Astropart. Phys., 05, 003 ([astro-ph/0412195](#))
- Moffat, J.W. 2005, preprint ([gr-qc/0506021](#))
- Perlmutter, S. *et al.* 1997, ApJ, 483, 565 ([astro-ph/9608192](#))
- Prada, F. *et al.* 2003, ApJ, 598, 260 ([astro-ph/0301360](#))
- Riess, A. G. *et al.* 1998, AJ, 113, 1009 ([astro-ph/9805201](#))
- Riess, A. G. *et al.* 2004, ApJ, 607, 665 ([astro-ph/0402512](#))
- Reuter, M. & Weyer, H. 2004, J. Cosmology Astropart. Phys., 12, 001 ([hep-th/0410119](#))
- Reuter, M. & Weyer, H. 2004, Phys. Rev. D69, 104022 ([hep-th/0311196](#))

- Romanowsky, A. J., Douglas, N. D., Arnaboldi, M., Kuijken, K, Merrifield, M. R., Napolitano, N. R., Capaccioli & M., Freeman, K. C. 2003, *Science*, 301, 1696 ([astro-ph/0308518](#))
- Romanowsky, A. J. *et al.* 2004, in Proc. IAU Symposium No. 220, *Dark matter in Galaxies*, ed. S. Ryder, D. J. Pisano, M. Walker & K. Freedman, (San Francisco: ASP) 165 ([astro-ph/0310874](#))
- Sanders, R. H. 1996, *ApJ*, 473, 117 ([astro-ph/9606089](#))
- Sanders, R. H. 2005, preprint ([astro-ph/0502222](#))
- Sanders, R. H. & McGaugh, S. S. 2002, *ARA&A*40, 263 ([astro-ph/0204521](#))
- Sanders, R. H. & Verheijen, M. A. W. 1998, *ApJ*, 503, 97 ([astro-ph/9802240](#))
- Shapiro, I. L., Sola, J. & Stefancic, H. 2005, *J. Cosmology Astropart. Phys.*, 01, 012 ([hep-ph/0410095](#))
- Sheldon, E. S. *et al.* 2003, *AJ*, 127, 2544 ([astro-ph/0312036](#))
- Sofue, Y. 1996, *ApJ*, 458, 120 ([astro-ph/9507098](#))
- Spergel, D. N. *et al.* 2003, *ApJS*, 148, 175 ([astro-ph/0302209](#))
- Tully, R. B. 1988, *Nearby Galaxies Catalog* (Cambridge, Cambridge University Press)
- Tully, R. B. & Fisher, J. R. 1977, *A&A*, 54, 661
- Verheijen, M. A. W. 2001, *ApJ*, 563, 694 ([astro-ph/0108225](#))
- Verheijen, M. A. W. & Sancisi, R. 2001, *A&A*, 370, 765 ([astro-ph/0101404](#))

Fig. 1.— Photometric Fits to Galaxy Rotation Curves: There are 58 galaxies presented here, each is a best fit via the single parameter $(M/L)_{\text{stars}}$ based on the photometric data of the gaseous (HI plus He) and luminous stellar disks. The 29 galaxies labeled *UMa* are members of the Ursa Major cluster of galaxies. For the UMa subset, available *K*-band data was used to reproduce the velocity profiles of the gaseous disk (HI plus He) distribution and luminous stellar disks accounting for the revised distance estimate to UMa from 15.5 Mpc to 18.6 Mpc according to Verheijen & Sancisi (2001). The numerical results of the UMa fits are presented in Table 2. In all cases, the radial coordinate (horizontal axis) is given in kpc and the rotation velocity (vertical axis) in km/s. The red points with error bars are the observations, the solid black line is the rotation curve determined from MSTG, the dash-dot cyan line is the rotation curve determined from MOND. The other curves are the Newtonian rotation curves of the various separate components: the long dashed green line is the rotation curve of the gaseous disk (HI plus He); the dotted magenta curve is that of the luminous stellar disk.

Fig. 2.— Parametric Fits to Galaxy Rotation Curves: There are 101 galaxies presented here – the *complete sample* of galaxies of Table 1. These rotation curves are best fit to the parametric mass distribution (independent of luminosity observations) of equations (17) and (18) – a two parameter fit to the total galactic Mass, M , and a core radius, r_c . In all cases, the red points (with error bars) are the observations. In those cases where the high resolution observations connect together, error bars if available are shown as region specific. The solid black line is the rotation curve determined from MSTG, the dash-dot cyan line is the rotation curve determined from MOND. The horizontal dotted black line is the MSTG predicted value of the measured “flat rotation velocity”, v_0 of equation (35). The remaining curve – the short dashed blue line is the Newtonian galaxy rotation curve. The numerical results of the fits are presented in Table 3.

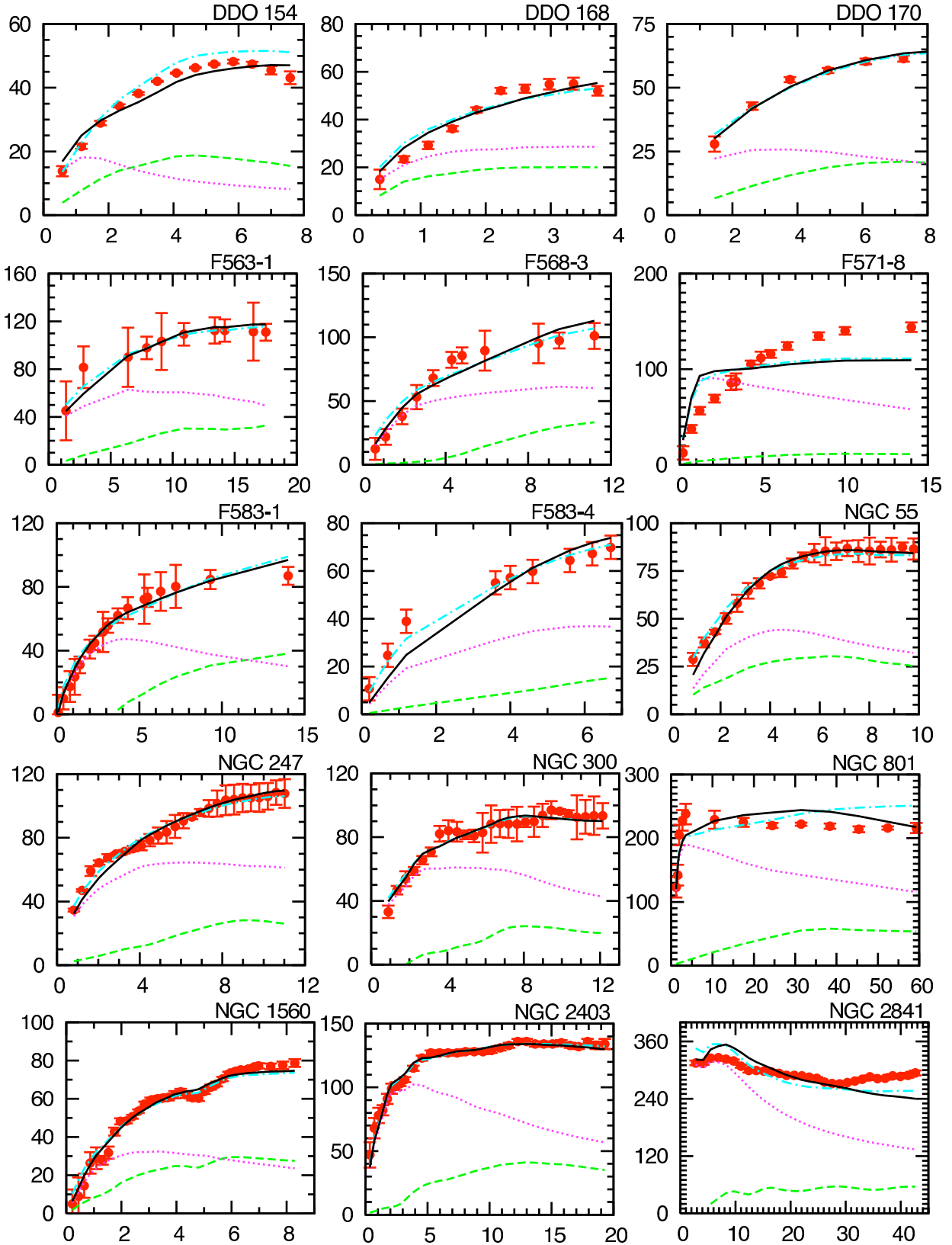


Fig. 1.— Photometric Galaxy Rotation Curve Fits

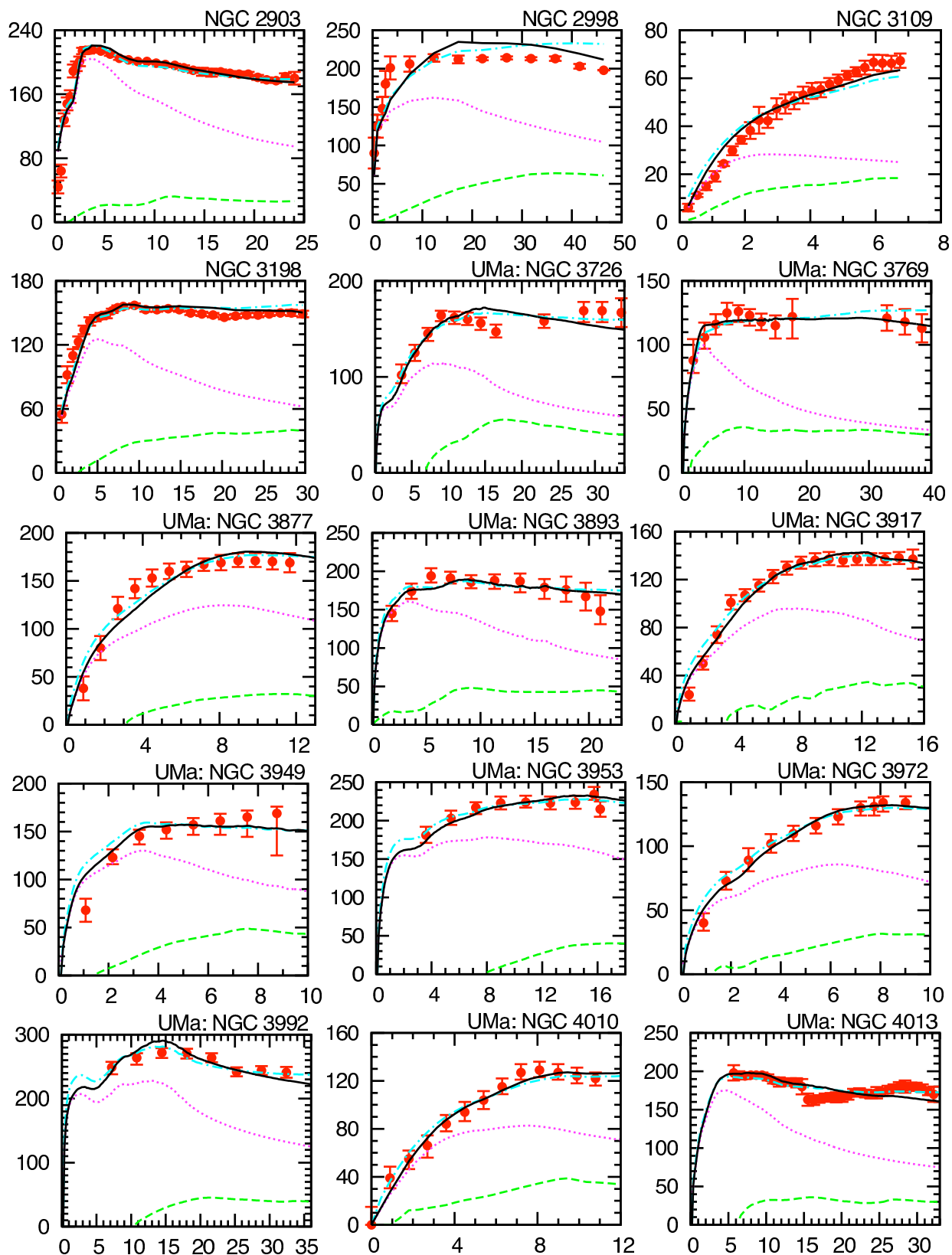


Fig. 1 Continued.— Photometric Galaxy Rotation Curve Fits

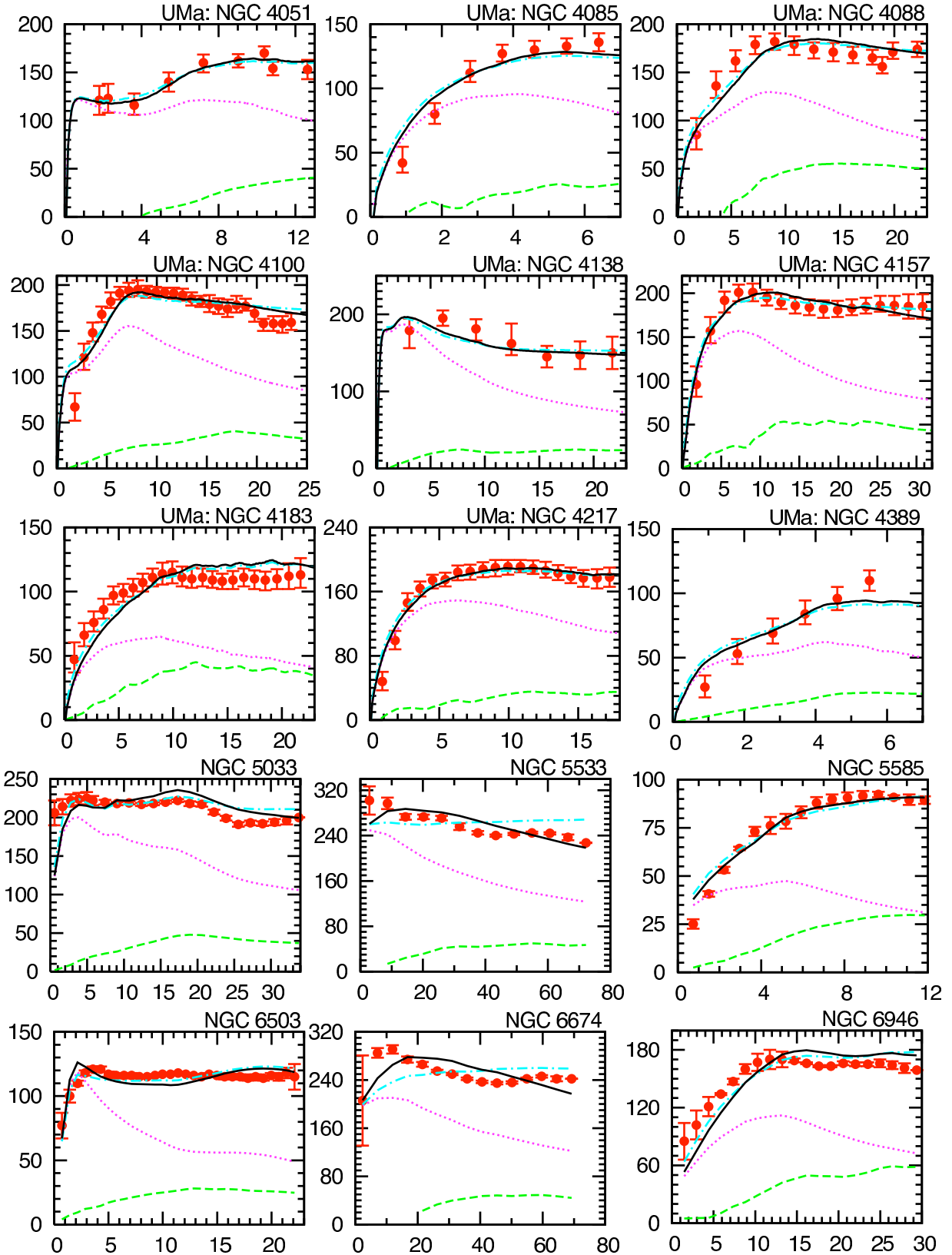


Fig. 1 Continued.— Photometric Galaxy Rotation Curve Fits

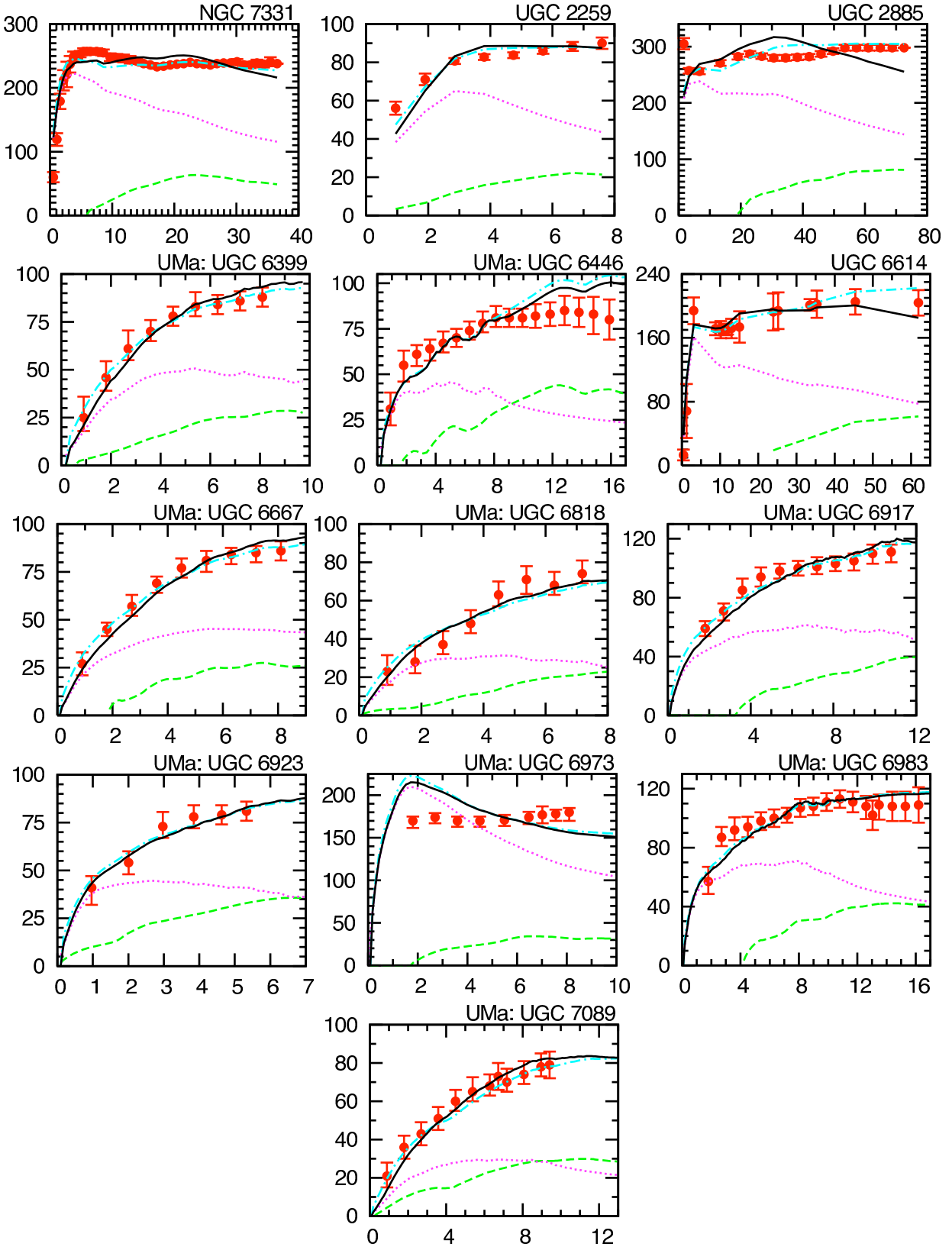


Fig. 1 Continued.— Photometric Galaxy Rotation Curve Fits

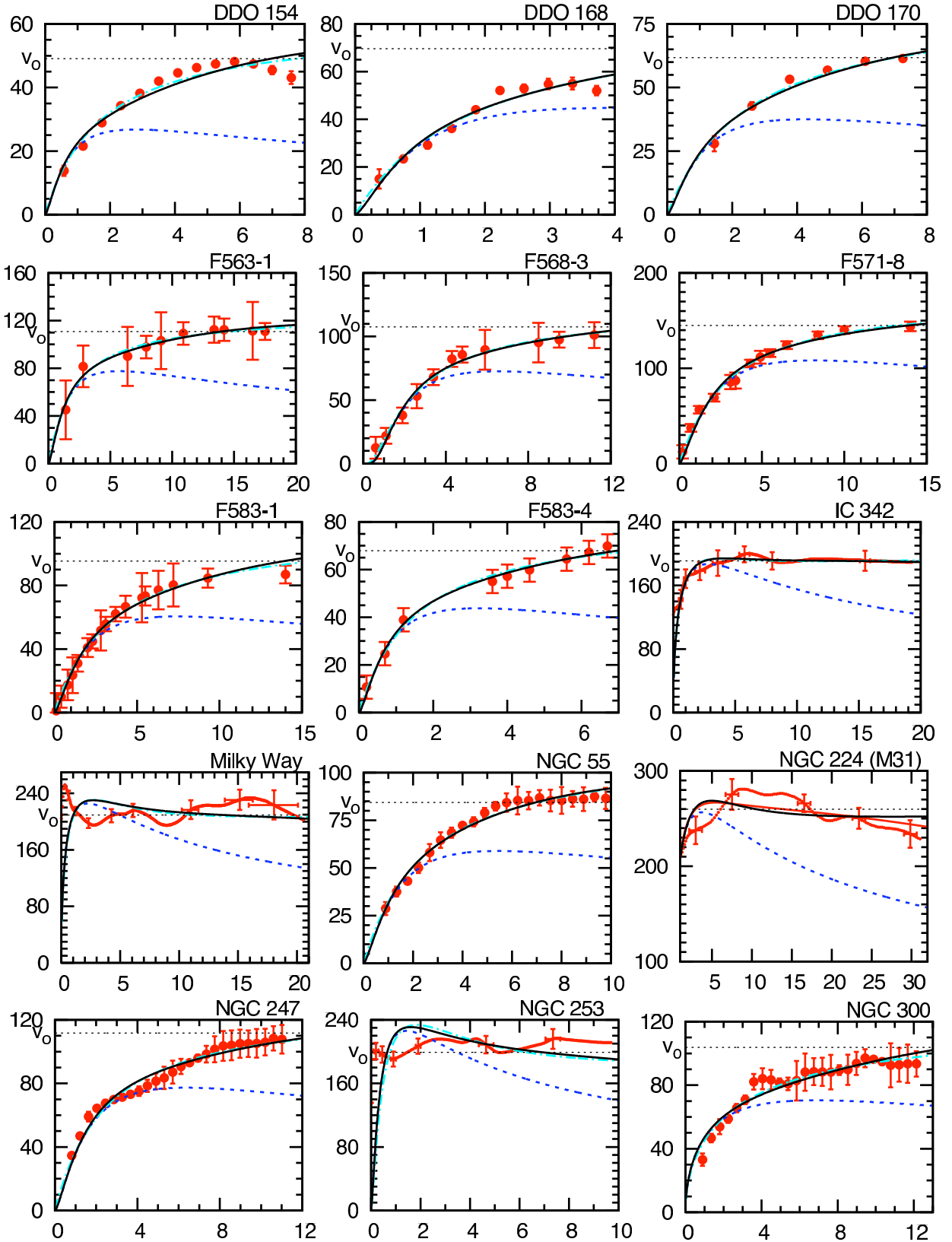


Fig. 2.— Parametric Galaxy Rotation Curve Fits

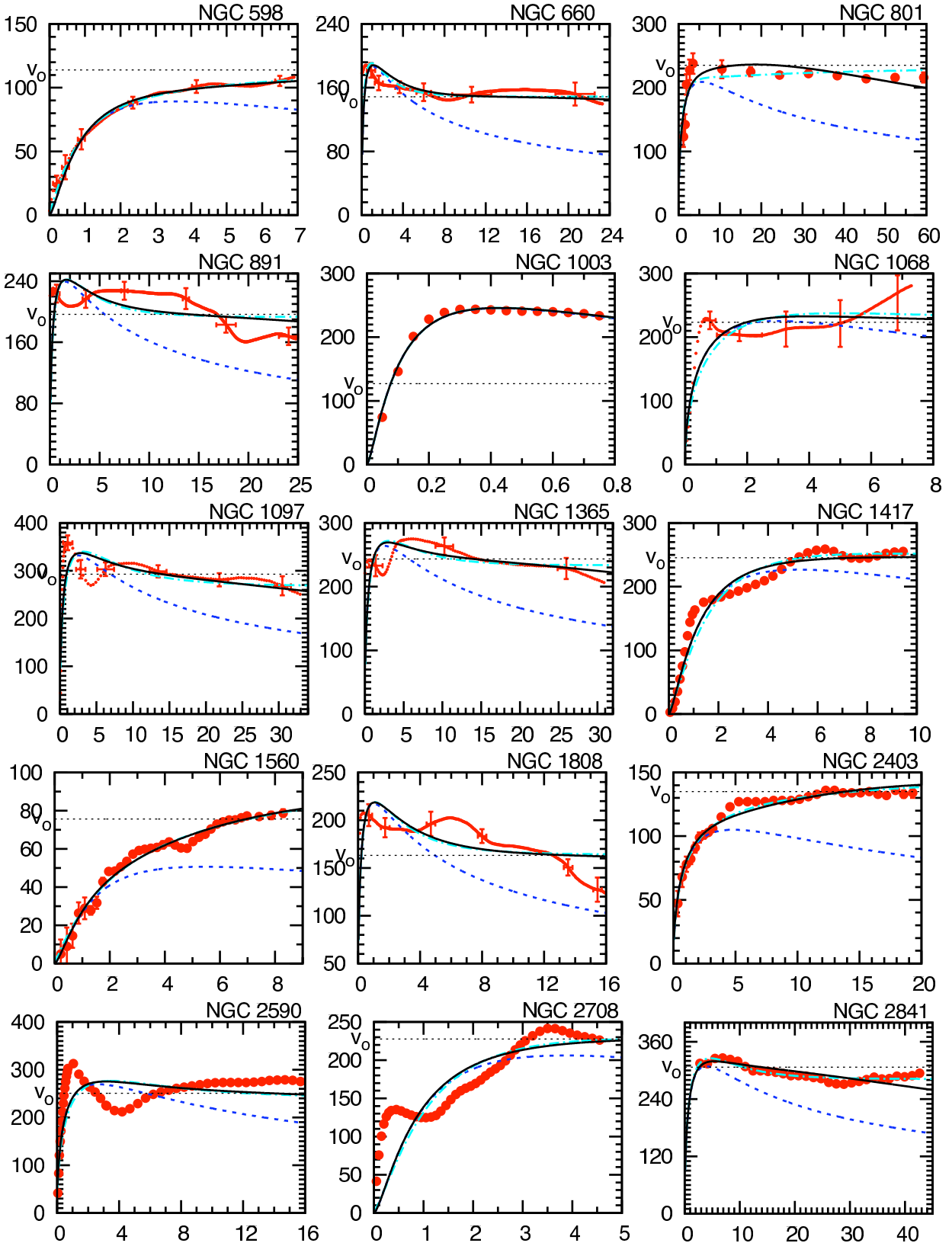


Fig. 2 Continued.— Parametric Galaxy Rotation Curve Fits

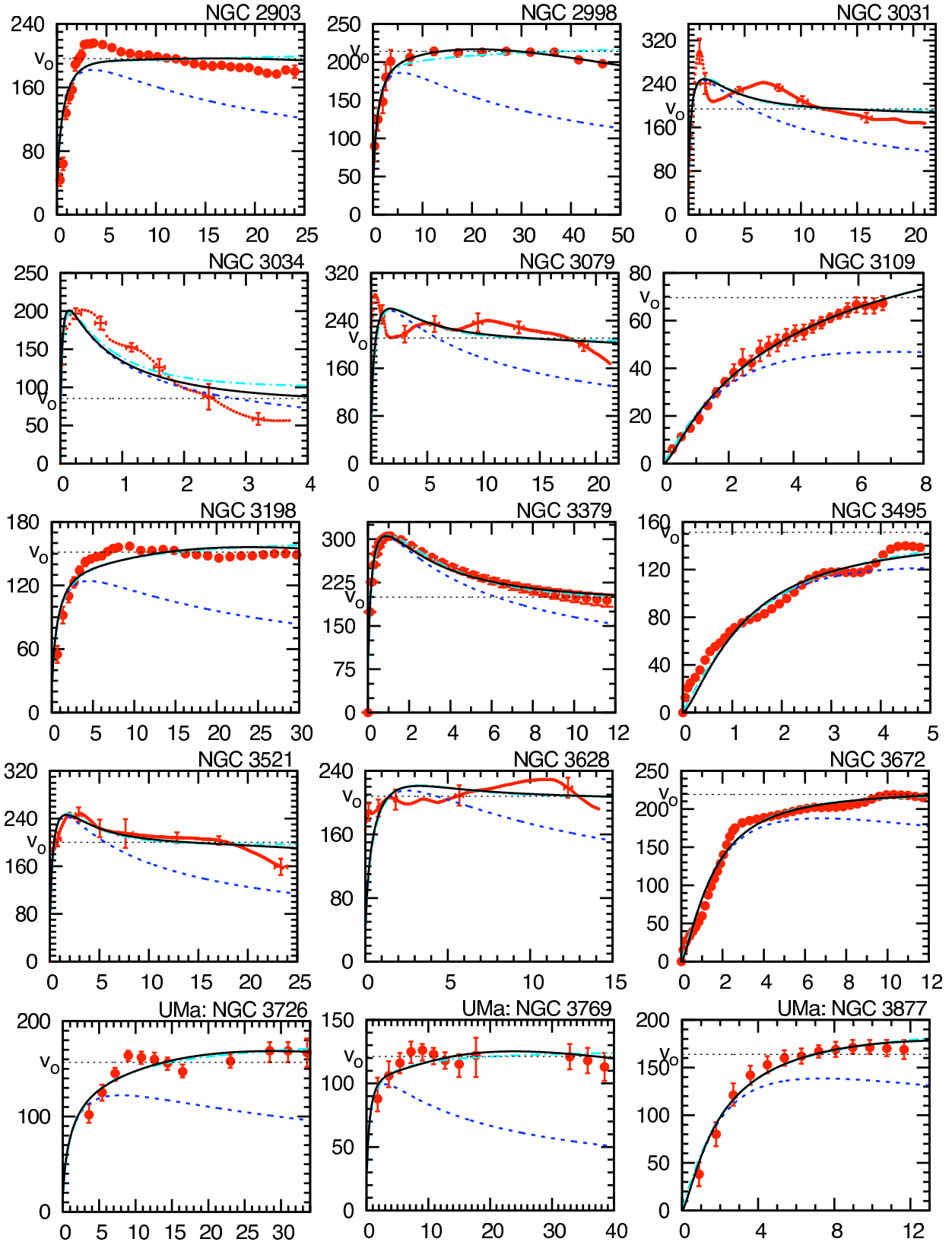


Fig. 2 Continued.— Parametric Galaxy Rotation Curve Fits

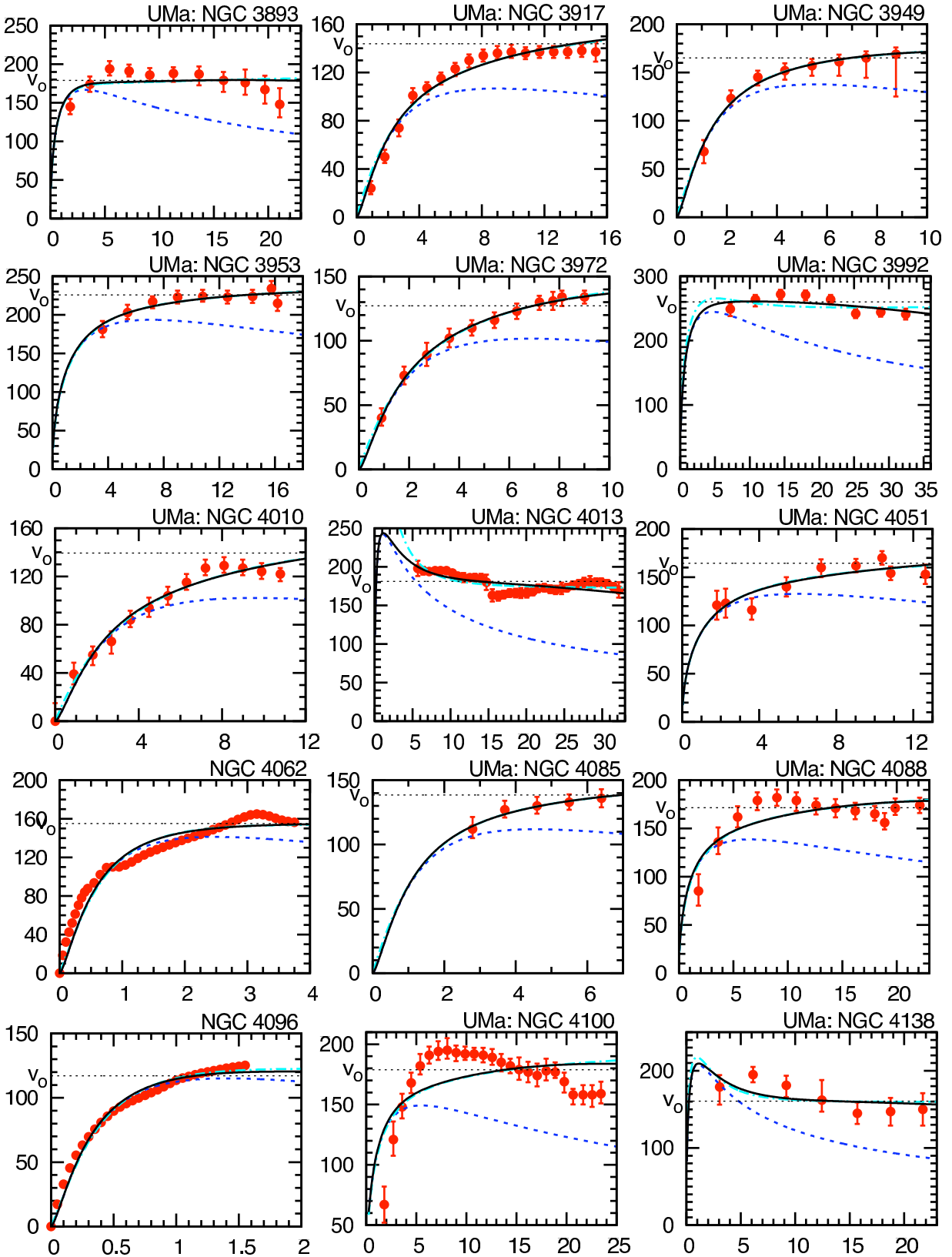


Fig. 2 Continued.— Parametric Galaxy Rotation Curve Fits

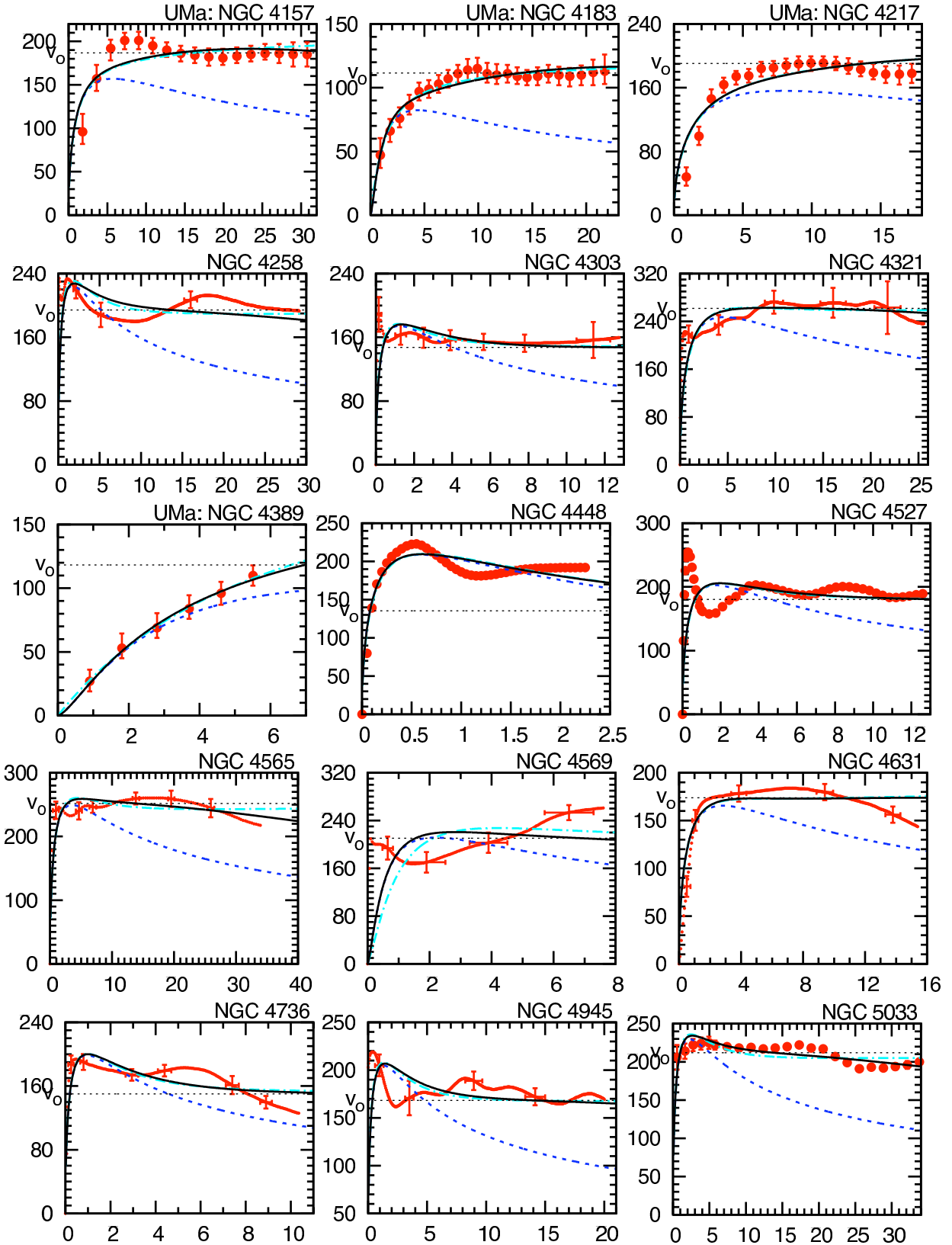


Fig. 2 Continued.— Parametric Galaxy Rotation Curve Fits

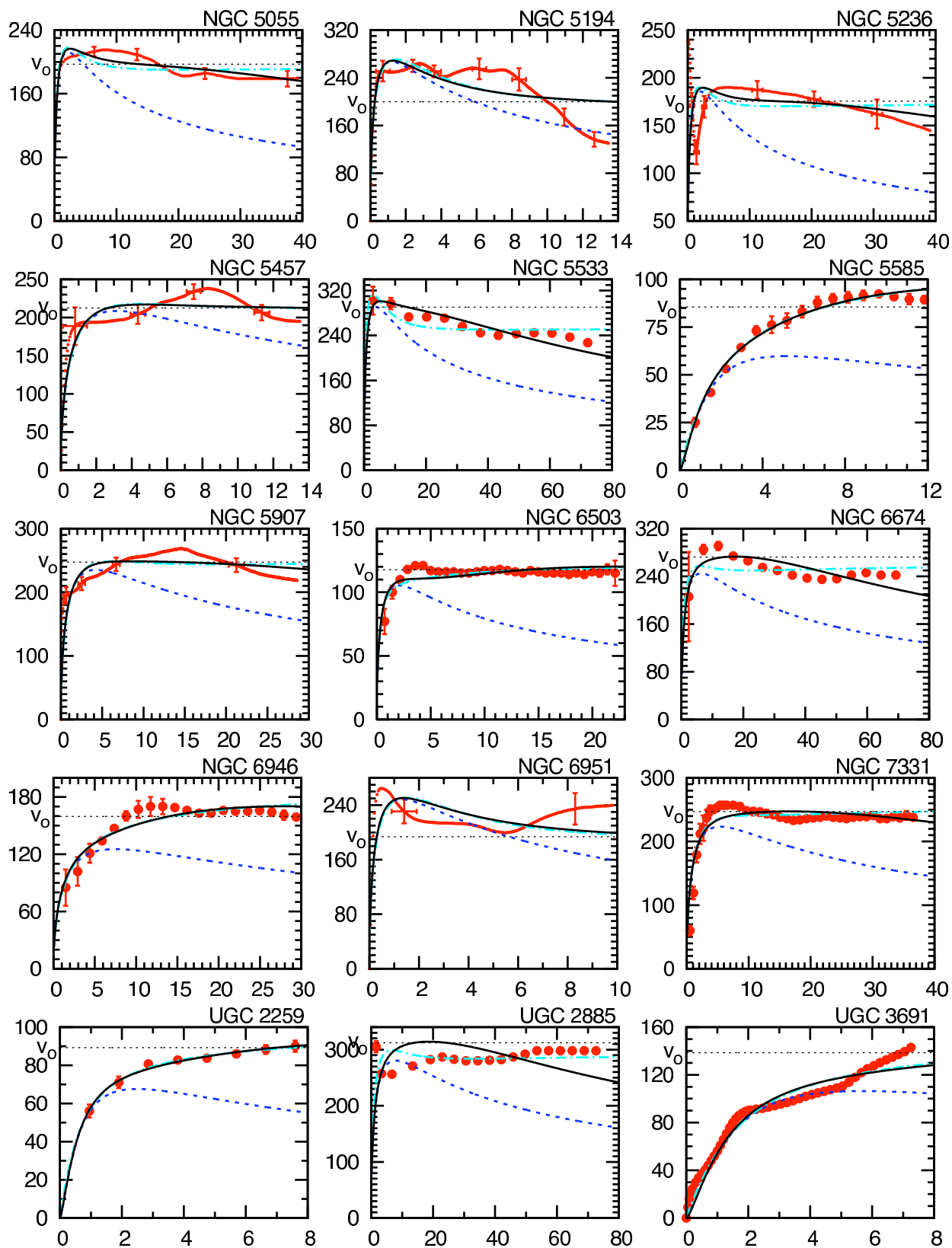


Fig. 2 Continued.— Parametric Galaxy Rotation Curve Fits

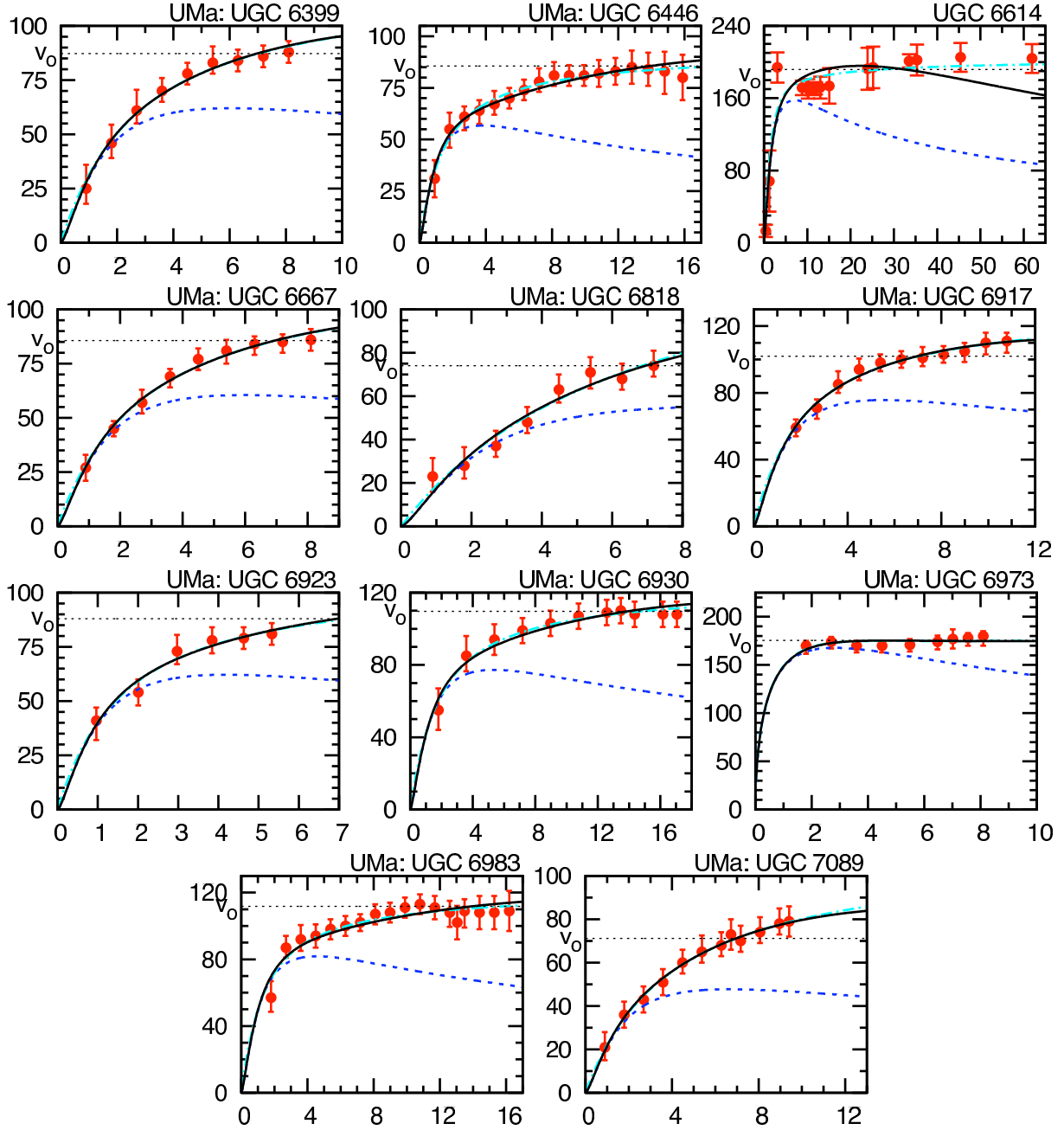


Fig. 2 Continued.— Parametric Galaxy Rotation Curve Fits

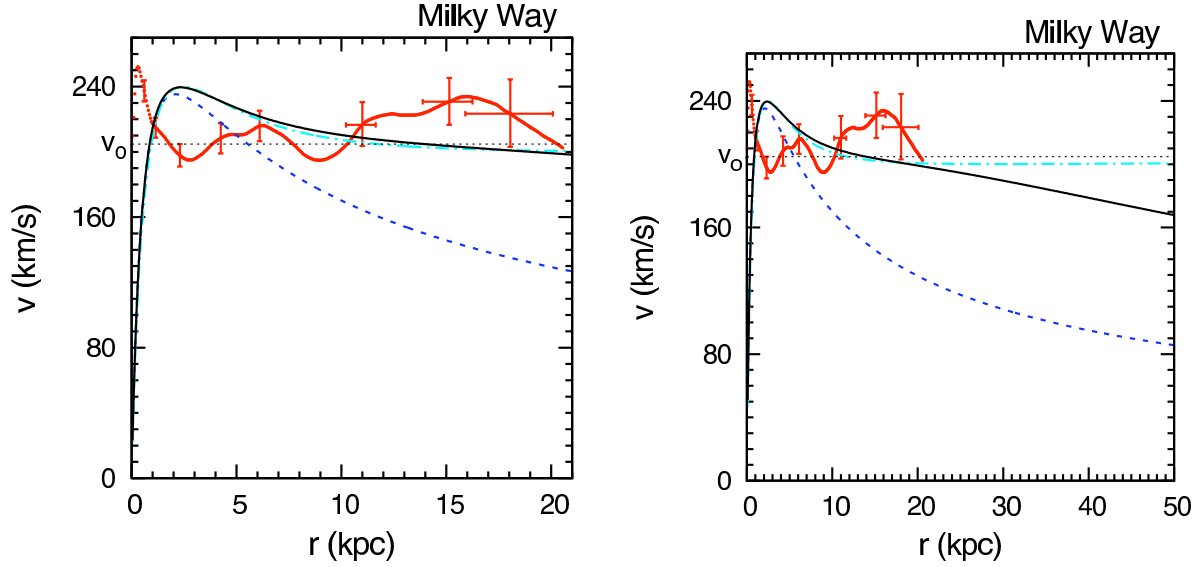


Fig. 3.— High Resolution rotation curve for the Milky Way. Both rotation curves are the same best fit to a parametric mass distribution (independent of luminosity observations) – a two parameter fit to the total galactic mass, M , and a core radius, r_c . The red points are the observations – error bars are shown as region specific. The solid black line is the rotation curve determined from MSTG, the dash-dot cyan line is the rotation curve determined from MOND. The horizontal dotted black line is the MSTG predicted value of the measured “flat rotation velocity”, v_0 of equation equation (35). The remaining curve – the short dashed blue line is the Newtonian galaxy rotation curve. The first rotation curve (leftmost) is plotted out to the edge of the visible stars in the galaxy at a distance of $r_{\text{out}} \approx 20.5$ kpc. The second rotation curve (rightmost) is plotted out to 50 kpc in order to distinguish the MSTG and MOND predictions. The numerical results of the fit are presented in Table 3.

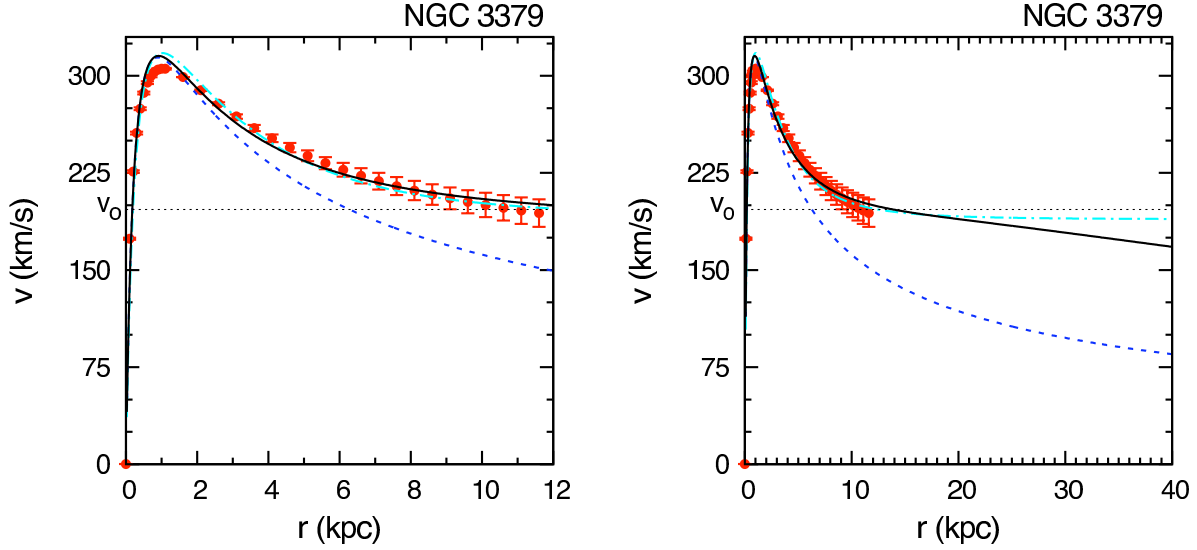


Fig. 4.— Rotation curve for the elliptical galaxy NGC 3379. Both rotation curves are the same best fit to a parametric mass distribution (independent of luminosity observations) – a two parameter fit to the total galactic Mass, M , and a core radius, r_c . The red points (with error bars) are samplings of the circular velocity profile constrained by orbit modeling according to Romanowsky *et al.* (2003, 2004). The solid black line is the rotation curve determined from MSTG, the dash-dot cyan line is the rotation curve determined from MOND. The horizontal dotted black line is the MSTG predicted value of the measured “flat rotation velocity”, v_0 of equation (35). The remaining curve – the short dashed blue line is the Newtonian galaxy rotation curve. The first rotation curve (leftmost) is plotted out to the edge of the visible stars in the galaxy at a distance of $r_{\text{out}} \approx 12$ kpc. The second rotation curve (rightmost) is plotted out to 40 kpc in order to distinguish the MSTG and MOND predictions. The numerical results of the fit are presented in Table 3.

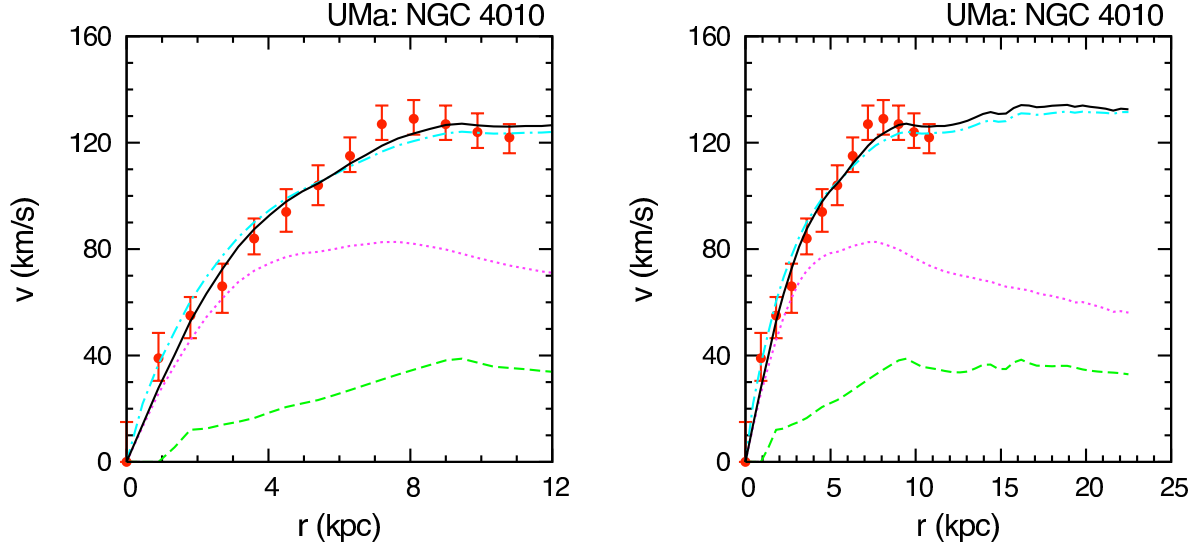


Fig. 5.— Rotation curve for NGC 4010 in the Ursa Major cluster of galaxies reproduced from the original photometry of Verheijen (2001); Verheijen & Sancisi (2001) – accounting for the revised distance estimate to UMa from 15.5 Mpc to 18.6 Mpc. Both rotation curves are the same best fit via the single parameter $(M/L)_{\text{stars}}$ based on the K -band photometric observations of the gaseous (HI plus He) and luminous stellar disks for MSTG and MOND. In every case, the radial coordinate (horizontal axis) is given in kpc and the rotation velocity (vertical axis) in km/s. The red points with error bars are the observations, the solid black line is the rotation curve determined from MSTG, the dash-dot cyan line is the rotation curve determined from MOND. The other curves are the Newtonian rotation curves of the various separate components: the long dashed green line is the rotation curve of the gaseous disk (HI plus He); the dotted magenta curve is that of the luminous stellar disk. The first rotation curve (leftmost) is plotted out to the edge of the visible stars in the galaxy at a distance of $r_{\text{out}} \approx 10.8$ kpc. The second rotation curve (rightmost) is plotted out to ≈ 23 kpc – the extent of the HI and K -band data – in order to extend and distinguish the MSTG and MOND “flat rotation velocity” predictions. The numerical results of the fit are presented in Table 2.

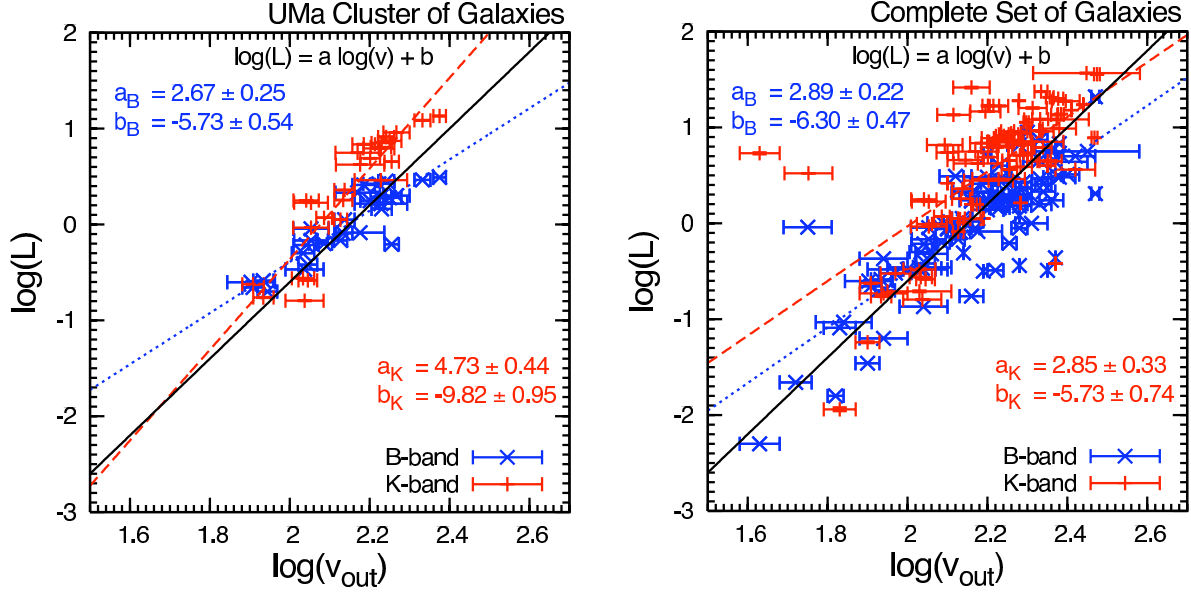


Fig. 6.— Observed B - and K -band Tully-Fisher relation for the UMA cluster of galaxies, and the *complete sample* of galaxies. The vertical axis is the (base 10) logarithm of the observed galaxy luminosity (in $10^{10}L_{\odot}$); and the horizontal axis is the (base 10) logarithm of the observed rotational velocity (in km/s) at the maximum observed radius. In both plots, the blue \times -points are the observed B -band luminosity data and the red $+$ -points are the observed K -band luminosity data. In all cases, the Tully-Fisher relation is parametrized by $\log(L) \equiv a \log(v) + b$. In both plots, the blue dotted lines are the best fit B -band Tully-Fisher relation and the red dashed lines are the best fit K -band Tully-Fisher relation. The best fit results using a nonlinear least-squares fitting routine including estimated errors are summarized in Table 4. The solid black line is the MOND prediction with $\langle M/L \rangle \equiv 1$.

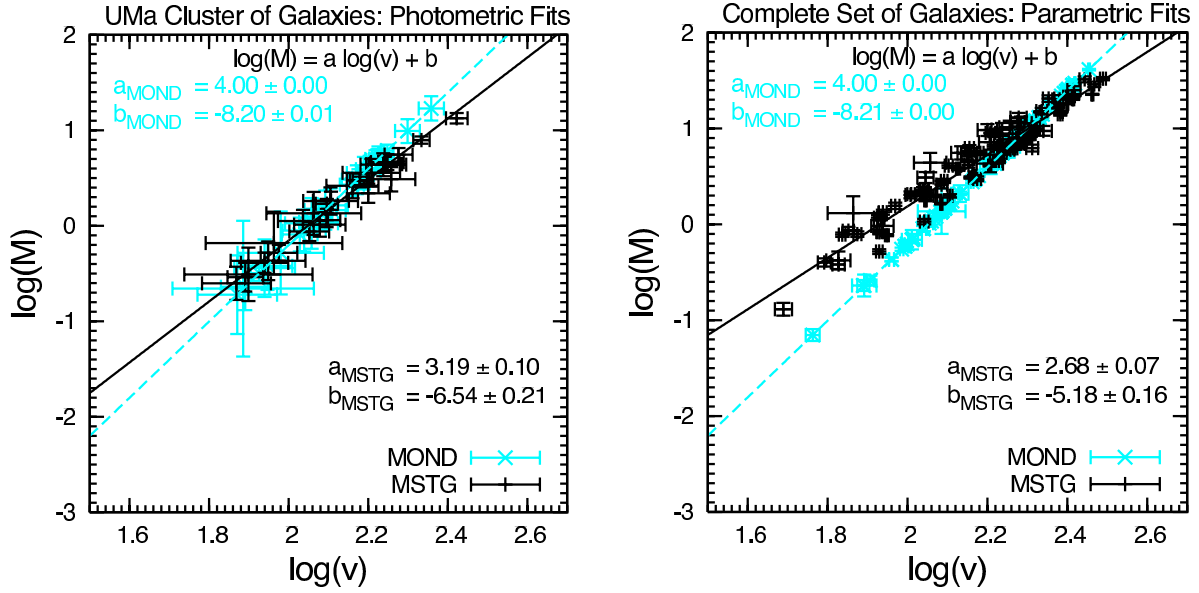


Fig. 7.— Actual Tully-Fisher relation for the UMa cluster of galaxies’ photometry, and the *complete sample* of galaxies resulting from the parametric fits. The first curve (leftmost) is the combined HSB, LSB and Dwarf galaxies fit to the photometric data of the UMa cluster of galaxies corresponding to those galaxies of Fig. 1 labeled by *UMa* and Table 2. The second curve (rightmost) is the combined HSB, LSB and Dwarf galaxies fit to the parametric data of the *complete sample* corresponding to Fig. 2 and Table 3. The vertical axes are the (base 10) logarithm of the total mass of the galaxy (in $10^{10}M_{\odot}$) resulting from the fits. The horizontal axes are the (base 10) logarithm of the flat rotational velocity (in km/s) as determined from the fits – v_0 in MSTG and v_c in MOND. In all plots, the cyan \times -points are the MOND results, and the black $+$ -points are the MSTG results. In all cases, the Tully-Fisher relation is parametrized by $\log(M) \equiv a \log(v) + b$; and the results of the fits are shown for MSTG and MOND. The dashed cyan line is the best fit solution for the MOND results, and the solid black line is the best fit solution for MSTG results. The best fit results using a nonlinear least-squares fitting routine including estimated errors are summarized in Table 4.

Table 1. GALAXY PROPERTIES OF THE *Complete Sample*

Galaxy	Type	Surface Brightness	L_B ($10^{10}L_\odot$)	L_K ($10^{10}L_\odot$)	r_{out} (kpc)	v_{out} (km s^{-1})	Distance (Mpc)	Redshift	Ref
(1)	(2)	(3)	(4)	(5)	(6)	(7)	(8)	(9)	(10)
DDO 154	IB	LSB	0.005	5.392	7.6	43.1 ± 2.0	4.0	0.000103	1
DDO 168	Irr	LSB	0.022	...	3.7	52.0 ± 2.0	3.8	0.000640	2
DDO 170	Im	...	0.016	...	9.6	66.0 ± 1.0	12.0	0.003119	1
F563-1	Sm	LSB	0.135	0.100	17.5	110.9 ± 7.0	45.0	...	3
F568-3	Sd	LSB	0.331	0.272	11.2	101.0 ± 10.2	77.0	...	3
F571-8	...	LSB	0.174	...	14.0	143.9 ± 5.0	48.0	...	3
F583-1	Sm	LSB	0.063	0.054	14.0	86.9 ± 5.6	32.0	...	3
F583-4	Sc	LSB	0.093	0.072	6.7	69.9 ± 4.9	49.0	...	3
IC 342	Sc	HSB	6.607	5.126	19.3	191.1 ± 12.7	3.9	0.000103	4
Milky Way	Sb	HSB	20.5	$202.6^{+21.1}_{-20.3}$	4
NGC 55	SBm	LSB	0.430	0.187	9.8	86.5 ± 5.5	1.6	0.000430	2
NGC 224	Sb	HSB	1.738	4.443	31.3	227.9 ± 14.5	0.7	-0.001001	4
NGC 247	SBc	LSB	0.350	0.193	11.0	107.8 ± 9.0	2.8	0.000520	2
NGC 253	Sc	HSB	1.585	4.482	9.7	211.5 ± 12.5	2.5	0.000811	4
NGC 300	Sc	HSB	0.300	0.300	12.1	93.4 ± 8.0	2.2	0.000480	2
NGC 598	Sc	LSB	0.331	0.330	6.9	108.1 ± 4.0	0.8	-0.000597	4
NGC 660	Sc	HSB	1.047	4.557	23.3	139.6 ± 14.5	13.0	0.002835	4
NGC 801	Sc	HSB	7.400	23.640	59.0	216.0 ± 8.0	80.0	0.019227	2
NGC 891	Sb	HSB	1.514	7.733	24.8	164.6 ± 11.5	8.9	0.001761	4
NGC 1003	Scd	LSB	0.437	0.382	0.8	233.6 ^a	9.5	0.002088	4
NGC 1068	Sb	HSB	5.623	36.796	7.3	$280.8^{+27.7}_{-86.5}$	18.1	0.003793	4
NGC 1097	SBb	HSB	3.236	18.762	33.2	249.1 ± 20.0	16.0	0.004240	4
NGC 1365	SBb	HSB	1.000	15.974	31.1	205.7 ± 16.7	15.6	0.005457	4
NGC 1417	Sb	LSB	...	15.200	9.6	255.7 ^a	54.1	0.013569	4
NGC 1560	Sd	LSB	0.035	0.058	8.3	78.7 ± 2.0	3.0	-0.000120	1
NGC 1808	SBc	HSB	1.000	6.559	16.0	123.8 ± 12.7	11.4	0.003319	4
NGC 2403	Sc	HSB	0.790	0.816	19.3	134.0 ± 4.0	3.3	0.000437	1
NGC 2590	Sb	HSB	...	17.278	15.8	275.2 ^a	64.5	0.016665	4
NGC 2708	Sb	HSB	0.324	3.952	4.6	225.7 ^a	24.6	0.006698	4
NGC 2841	Sb	HSB	2.050	7.797	42.7	294.0 ± 5.0	9.5	0.002128	1
NGC 2903	Sc	HSB	1.530	3.654	24.0	180.0 ± 8.0	6.4	0.001855	1
NGC 2998	SBc	HSB	9.000	11.288	46.4	198.0 ± 3.0	67.0	0.015958	2
NGC 3031	Sb	HSB	0.324	7.167	21.1	167.4 ± 9.0	3.3	-0.000113	4
NGC 3034	I	HSB	0.912	3.327	3.7	56.5 ± 7.8	3.3	0.000677	4
NGC 3079	Sc	HSB	3.981	7.032	21.3	167.9 ± 9.6	15.6	0.003723	4
NGC 3109	SBm	LSB	0.081	0.011	6.7	67.3 ± 3.0	1.6	0.001344	1
NGC 3198	Sc	HSB	0.900	1.570	29.7	149.0 ± 3.0	9.4	0.002212	1
NGC 3379	E	HSB	0.891	8.712	12.0	192.5 ± 11.0	11.0	0.003039	6
NGC 3495	Sd	LSB	0.490	1.018	4.8	138.5 ^a	12.8	0.003789	4
NGC 3521	SBb	HSB	1.380	14.648	23.6	156.8 ± 13.6	11.4	0.002672	4
NGC 3628	Sb/I	HSB	1.514	3.871	14.2	192.0 ± 12.7	6.7	0.002812	4
NGC 3672	Sc	LSB	4.571	9.267	11.8	214.7 ^a	28.4	0.006211	4
NGC 3726	SBc	HSB	2.650	6.216	33.6	167.0 ± 15.0	18.6	0.002887	5
NGC 3769	SBb	HSB	0.680	1.678	38.5	113.0 ± 11.0	18.6	0.002459	5

Table 1—Continued

Galaxy	Type	Surface Brightness	L_B ($10^{10} L_\odot$)	L_K ($10^{10} L_\odot$)	r_{out} (kpc)	v_{out} (km s^{-1})	Distance (Mpc)	Redshift	Ref
(1)	(2)	(3)	(4)	(5)	(6)	(7)	(8)	(9)	(10)
NGC 3877	Sc	HSB	1.940	6.396	11.7	169.0 ± 10.0	18.6	0.002987	5
NGC 3893	Sc	HSB	2.140	5.598	21.1	148.0^{+21}_{-17}	18.6	0.003226	5
NGC 3917	Scd	LSB	1.120	2.289	15.3	137.0 ± 8.0	18.6	0.003218	5
NGC 3949	Sbc	HSB	1.650	2.901	8.8	169.0^{+7}_{-44}	18.6	0.002669	5
NGC 3953	SBbc	HSB	2.910	12.183	16.2	215.0 ± 10.0	18.6	0.003510	5
NGC 3972	Sbc	HSB	0.680	1.124	9.0	134.0 ± 5.0	18.6	0.002843	5
NGC 3992	SBbc	HSB	3.100	13.482	36.0	237.0^{+7}_{-10}	18.6	0.003496	5
NGC 4010	SBd	LSB	0.630	1.169	10.8	122.0^{+5}_{-6}	18.6	0.003008	5
NGC 4013	Sb	HSB	1.450	7.090	32.2	170.0 ± 10.0	18.6	0.002773	5
NGC 4051	SBbc	HSB	2.580	6.856	12.6	153.0 ± 10.0	18.6	0.002336	5
NGC 4062	Sc	HSB	0.316	1.131	3.8	156.3 ^a	9.7	0.002565	4
NGC 4085	Sc	HSB	0.810	1.797	6.4	136.0 ± 7.0	18.6	0.002487	5
NGC 4088	SBc	HSB	2.830	8.176	22.1	174.0 ± 8.0	18.6	0.002524	5
NGC 4096	Sc	HSB	0.891	2.610	1.6	125.3 ^a	12.2	0.001888	4
NGC 4100	Sbc	HSB	1.770	4.909	23.5	159.0^{+10}_{-8}	18.6	0.003584	5
NGC 4138	Sa	HSB	0.820	4.203	21.7	150.0 ± 21.0	18.6	0.002962	5
NGC 4157	Sb	HSB	2.000	9.098	30.8	185.0 ± 14.0	18.6	0.002583	5
NGC 4183	Scd	LSB	0.900	0.924	21.7	113.0^{+13}_{-10}	18.6	0.003102	5
NGC 4217	Sb	HSB	1.900	7.442	17.3	178.0 ± 12.0	18.6	0.003426	5
NGC 4258	SBc	HSB	2.692	6.579	29.2	193.1 ± 10.6	6.6	0.001494	4
NGC 4303	Sc	HSB	3.020	2.793	12.8	159.6 ± 22.5	8.1	0.005224	4
NGC 4321	Sc	HSB	4.365	12.102	25.6	236.1 ± 44.0	15.0	0.005240	4
NGC 4389	SBbc	HSB	0.610	1.782	5.5	110.0 ± 8.0	18.6	0.002396	5
NGC 4448	SBab	HSB	0.363	1.634	2.3	192.0 ^a	9.7	0.002205	4
NGC 4527	Sb	HSB	1.202	18.974	12.8	190.0 ^a	22.0	0.005791	4
NGC 4565	Sb	HSB	2.138	9.099	34.1	217.2 ± 14.4	10.2	0.004103	4
NGC 4569	Sab	HSB	5.012	3.621	7.6	260.9 ± 12.5	8.2	-0.000784	4
NGC 4631	Sc/I	HSB	1.738	1.111	15.4	143.5 ± 8.5	4.3	0.002021	4
NGC 4736	Sab	HSB	0.871	5.460	10.4	125.8 ± 7.9	5.1	0.001027	4
NGC 4945	Sc/I	HSB	2.818	16.740	20.0	169.6 ± 9.0	6.7	0.001878	4
NGC 5033	Sc	HSB	1.900	5.420	33.8	200.0 ± 5.0	11.9	0.002919	2
NGC 5055	SBc	HSB	1.778	8.467	39.4	179.0 ± 10.0	8.0	0.001681	4
NGC 5194	Sc	HSB	3.090	13.515	13.5	130.4 ± 12.3	9.6	0.001544	4
NGC 5236	SBc	HSB	2.089	26.057	39.3	144.4 ± 15.2	8.9	0.001711	4
NGC 5457	Sc	HSB	2.344	7.012	13.5	195.0 ± 10.2	7.2	0.000804	4
NGC 5533	Sab	HSB	5.600	20.604	72.2	227.0 ± 5.0	54.0	0.012896	2
NGC 5585	SBcd	HSB	0.240	0.212	11.9	89.4 ± 2.0	7.6	0.001017	2
NGC 5907	Sc	HSB	2.570	6.181	28.6	218.5 ± 10.8	11.6	0.002225	4
NGC 6503	Sc	HSB	0.480	0.985	22.1	115.0 ± 10.0	5.9	0.000200	1
NGC 6674	SBb	HSB	6.800	13.757	69.2	242.0 ± 4.0	49.0	0.011438	2
NGC 6946	SABcd	HSB	5.300	16.792	29.4	159.0 ± 5.0	10.1	0.000160	2
NGC 6951	Sbc	HSB	3.020	9.741	9.8	239.7 ± 23.1	18.0	0.004750	4
NGC 7331	Sb	HSB	5.400	19.969	36.0	238.0 ± 7.0	14.9	0.002722	1
UGC 2259	SBcd	HSB	0.100	0.008	7.6	90.0 ± 3.0	9.8	0.001945	1

Table 1—Continued

Galaxy	Type	Surface Brightness	L_B ($10^{10}L_\odot$)	L_K ($10^{10}L_\odot$)	r_{out} (kpc)	v_{out} (km s^{-1})	Distance (Mpc)	Redshift	Ref
(1)	(2)	(3)	(4)	(5)	(6)	(7)	(8)	(9)	(10)
UGC 2885	SBc	HSB	21.000	35.808	72.0	298.0 ± 5.0	79.0	0.019353	2
UGC 3691	Scd	HSB	1.698	1.573	7.2	144.1 ^a	30.0	0.007348	4
UGC 6399	Sm	HSB	0.200	...	8.1	88.0 ± 5.0	18.6	0.002640	5
UGC 6446	Sd	LSB	0.250	...	15.9	80.0 ± 11.0	18.6	0.002149	5
UGC 6614	...	LSB	...	7.157	61.9	203.9 ± 16.0	85.0	0.021185	3
UGC 6667	Scd	LSB	0.260	0.173	8.1	86.0 ± 5.0	18.6	0.003246	5
UGC 6818	Sd	LSB	0.180	...	7.2	74.0^{+7}_{-5}	18.6	0.002696	5
UGC 6917	SBd	LSB	0.380	0.260	10.8	111.0^{+5}_{-7}	18.6	0.003038	5
UGC 6923	Sdm	LSB	0.220	0.237	5.3	81.0 ± 5.0	18.6	0.003556	5
UGC 6930	Sd	LSB	0.500	0.275	17.1	108.0 ± 7.0	18.6	0.002592	5
UGC 6973	Sab	HSB	0.620	4.513	8.1	180.0^{+5}_{-10}	18.6	0.002337	5
UGC 6983	SBcd	LSB	0.340	0.160	16.2	109.0 ± 12.0	18.6	0.003609	5
UGC 7089	Sdm	LSB	0.440	...	9.4	79.0 ± 7.0	18.6	0.002568	5

Note. — Relevant galaxy properties of the *complete sample*: Column (1) is the NGC/UGC galaxy number. Column (2) is the galaxy morphological type. Column (3) is the surface brightness – denoted LSB if the galaxy central surface brightness is low ($\mu_0 \gtrsim 23 \text{ mag/arcsec}^2$) or HSB if the galaxy central surface brightness is otherwise high. Column (4) is B -band luminosity data taken from the original references except for Sofue (1996) and Romanowsky *et al.* (2003) which are taken from Tully (1988); and Column (5) is the K -band luminosity data converted from the 2MASS K -band apparent magnitude via equation (38) except for the Schombert F-type galaxies, which are taken from the original reference. Column (6) is the outermost observed radial position in the rotation velocity data; and Column (7) is the observed velocity at the outermost observed radial position. Column (8) is the distance to the galaxy adopted from the original references; and Column (9) is the observed redshift taken from the NASA/IPAC Extragalactic Database. Column (10) provides the primary original references.

^aError bars were not part of the available high resolution rotation curve data for this galaxy.

References. — (1) Begeman, Broeils & Sanders 1991; (2) Sanders 1996; (3) de Blok & McGaugh 1998; (4) Verheijen & Sancisi 2001; (5) Sofue 1996; (6) Romanowsky 2003.

Table 2. UMA PHOTOMETRIC ROTATION CURVE FIT RESULTS

Galaxy	M_{gas} ($10^{10} M_{\odot}$)	z_0 (kpc)	\longleftarrow M_{disk} ($10^{10} M_{\odot}$)	MSTG M ($10^{10} M_{\odot}$)	\longrightarrow v_0 (km s^{-1})	\longleftarrow M_{disk} ($10^{10} M_{\odot}$)	MOND M ($10^{10} M_{\odot}$)	\longrightarrow v_c (km s^{-1})
(1)	(2)	(3)	(4)	(5)	(6)	(7)	(8)	(9)
Dwarf (LSB & HSB) Galaxies								
NGC 3877	0.21	0.56	2.86 ± 0.80	3.07 ± 0.90	180.9 ± 25.4	3.71 ± 1.00	3.92 ± 1.10	158.3 ± 11.0
NGC 3949	0.49	0.35	1.70 ± 0.42	2.19 ± 0.50	158.6 ± 19.7	2.22 ± 0.80	2.70 ± 0.75	144.2 ± 10.0
NGC 3972	0.18	0.39	0.97 ± 0.15	1.15 ± 0.20	124.6 ± 9.9	1.07 ± 0.40	1.25 ± 0.40	118.9 ± 9.4
NGC 4085	0.16	0.31	0.87 ± 0.26	1.03 ± 0.30	119.7 ± 17.8	0.94 ± 0.30	1.10 ± 0.35	115.1 ± 9.2
NGC 4389	0.08	0.29	0.35 ± 0.15	0.43 ± 0.20	88.8 ± 19.2	0.28 ± 0.30	0.36 ± 0.25	87.0 ± 15.3
UGC 6399	0.11	0.48	0.29 ± 0.08	0.41 ± 0.10	87.0 ± 11.9	0.20 ± 0.10	0.32 ± 0.06	84.3 ± 4.2
UGC 6667	0.12	0.58	0.40 ± 0.09	0.52 ± 0.10	94.5 ± 10.0	0.26 ± 0.20	0.38 ± 0.22	88.5 ± 12.7
UGC 6818	0.15	0.36	0.10 ± 0.04	0.25 ± 0.10	73.9 ± 14.7	0.04 ± 0.20	0.19 ± 0.18	74.3 ± 17.1
UGC 6923	0.12	0.26	0.17 ± 0.04	0.29 ± 0.10	77.8 ± 8.0	0.11 ± 0.10	0.23 ± 0.13	77.7 ± 10.9
UGC 7089	0.19	0.62	0.12 ± 0.09	0.31 ± 0.20	79.2 ± 29.4	0.03 ± 0.40	0.22 ± 0.36	76.9 ± 31.4
UGC 6917	0.29	0.58	0.58 ± 0.13	0.87 ± 0.20	112.7 ± 13.0	0.52 ± 0.30	0.81 ± 0.33	106.6 ± 11.0
LSB GALAXIES								
NGC 3917	0.27	0.62	1.56 ± 0.32	1.83 ± 0.40	127.7 ± 13.3	1.37 ± 0.70	1.64 ± 0.66	127.3 ± 12.7
UGC 6446	0.44	0.36	0.22 ± 0.17	0.66 ± 0.50	91.9 ± 36.3	0.08 ± 0.50	0.52 ± 0.52	95.5 ± 23.9
UGC 6983	0.42	0.53	0.70 ± 0.20	1.12 ± 0.30	108.7 ± 15.7	0.47 ± 0.40	0.89 ± 0.45	109.3 ± 13.7
NGC 4010	0.42	0.69	1.40 ± 0.44	1.82 ± 0.60	127.4 ± 20.2	1.06 ± 0.40	1.48 ± 0.38	123.9 ± 8.0
NGC 4183	0.53	0.64	0.82 ± 0.45	1.35 ± 0.70	115.6 ± 31.7	0.53 ± 0.70	1.06 ± 0.65	114.2 ± 17.5
HSB GALAXIES								

Table 2—Continued

Galaxy	M_{gas} ($10^{10} M_{\odot}$)	z_0 (kpc)	\longleftarrow	MSTG	\longrightarrow	\longleftarrow	MOND	\longrightarrow
			M_{disk} ($10^{10} M_{\odot}$)	M ($10^{10} M_{\odot}$)	v_0 (km s^{-1})	M_{disk} ($10^{10} M_{\odot}$)	M ($10^{10} M_{\odot}$)	v_c (km s^{-1})
(1)	(2)	(3)	(4)	(5)	(6)	(7)	(8)	(9)
NGC 3726	0.98	0.68	2.62 ± 0.87	3.59 ± 1.20	161.3 ± 26.9	2.59 ± 1.40	3.56 ± 1.40	154.5 ± 15.2
NGC 3769	0.68	0.36	1.02 ± 0.13	1.70 ± 0.20	124.7 ± 8.0	0.78 ± 0.70	1.46 ± 0.69	123.5 ± 14.7
NGC 3893	0.76	0.49	3.67 ± 0.66	4.43 ± 0.80	173.9 ± 15.7	4.24 ± 1.50	5.00 ± 1.52	168.2 ± 12.8
NGC 3953	0.43	0.77	7.47 ± 0.71	7.90 ± 0.70	215.6 ± 10.2	9.38 ± 2.80	9.81 ± 2.81	199.0 ± 14.3
NGC 3992	0.81	0.83	12.57 ± 1.58	13.39 ± 1.70	264.6 ± 16.6	16.15 ± 5.00	16.96 ± 4.96	228.2 ± 16.7
NGC 4013	0.45	0.41	4.19 ± 0.80	4.64 ± 0.90	176.9 ± 16.8	4.58 ± 0.70	5.03 ± 0.72	168.4 ± 6.0
NGC 4051	0.39	0.54	2.57 ± 0.29	2.96 ± 0.30	150.7 ± 8.4	2.65 ± 1.10	3.04 ± 1.06	148.5 ± 12.9
NGC 4088	1.12	0.67	3.24 ± 0.86	4.36 ± 1.20	172.9 ± 22.9	3.56 ± 1.30	4.68 ± 1.29	165.4 ± 11.4
NGC 4100	0.45	0.51	3.96 ± 0.82	4.41 ± 0.90	173.7 ± 18.1	4.43 ± 1.20	4.88 ± 1.25	167.1 ± 10.7
NGC 4138	0.21	0.28	2.78 ± 0.42	2.99 ± 0.50	151.1 ± 11.5	2.93 ± 0.70	3.14 ± 0.70	149.7 ± 8.4
NGC 4157	1.17	0.52	4.38 ± 0.71	5.55 ± 0.90	188.8 ± 15.3	4.96 ± 0.90	6.13 ± 0.88	176.9 ± 6.3
NGC 4217	0.37	0.58	4.12 ± 0.72	4.49 ± 0.80	174.8 ± 15.3	4.66 ± 1.10	5.03 ± 1.11	168.4 ± 9.3
UGC 6973	0.25	0.19	2.38 ± 0.72	2.63 ± 0.80	144.6 ± 21.7	2.66 ± 0.20	2.91 ± 0.16	146.9 ± 2.0

Note. — Best fit results of the UMa cluster of galaxies according to both MSTG and MOND via the single parameter $(M/L)_{stars}$ based on the K -band photometric data of the gaseous (HI plus He) and luminous stellar disks, corresponding to the fits (labeled UMa) of Fig. 1 and Fig. 5. Column (1) is the NGC/UGC galaxy number. Column (2) is the mass of the infinitely thin gaseous disk (HI plus He). Column (3) is the K -band vertical scale height of the luminous stellar disk. The MSTG best fit results are presented in Columns (4) - (6), where Column (4) is the best fit mass of the luminous stellar disk; Column (5) is the MSTG predicted total mass of the galaxy and is the sum of Column (2) and (4); and Column (6) is the predicted MSTG flat rotation velocity, v_0 , of equation (35). The MOND best results are presented in Columns (7) - (9), where Column (7) is the best fit mass of the luminous stellar disk; Column (8) is the MOND predicted mass of the galaxy and is the sum of Column (2) and (7); and Column (9) is the MOND asymptotic velocity, v_c of equation (31).

Table 3. PARAMETRIC ROTATION CURVE FIT RESULTS

Galaxy	\longleftarrow	MSTG	\longrightarrow	\longleftarrow	MOND	\longrightarrow
	M ($10^{10} M_{\odot}$)	r_c (kpc)	v_0 (km s^{-1})	M ($10^{10} M_{\odot}$)	r_c (kpc)	v_c (km s^{-1})
(1)	(2)	(3)	(4)	(5)	(6)	(7)
Dwarf (LSB & HSB) Galaxies						
DDO 154 ^a	0.13 ± 0.02	0.53 ± 0.07	48.9 ± 2.4	0.07 ± 0.01	0.95 ± 0.12	57.9 ± 2.3
DDO 168	0.42 ± 0.09	0.66 ± 0.08	67.1 ± 4.7	0.23 ± 0.06	0.89 ± 0.14	77.9 ± 5.5
DDO 170	0.40 ± 0.04	0.82 ± 0.07	61.9 ± 2.3	0.26 ± 0.03	1.38 ± 0.10	80.7 ± 1.9
F583-4	0.38 ± 0.04	0.57 ± 0.05	67.2 ± 2.4	0.23 ± 0.03	0.77 ± 0.1	77.5 ± 2.7
NGC 55	1.17 ± 0.07	0.99 ± 0.05	84.4 ± 2	0.91 ± 0.07	1.39 ± 0.08	109.7 ± 2.1
NGC 1560	0.79 ± 0.05	0.93 ± 0.04	74.9 ± 1.7	0.59 ± 0.05	1.43 ± 0.08	98.5 ± 2.2
NGC 2708	9.43 ± 1.1	0.66 ± 0.05	218.7 ± 10.8	12.97 ± 1.59	0.79 ± 0.06	213.4 ± 6.5
NGC 3109	0.78 ± 0.04	1.15 ± 0.04	68.6 ± 1.3	0.62 ± 0.04	2 ± 0.06	99.8 ± 1.5
NGC 3877	8.65 ± 0.53	1.31 ± 0.06	164.8 ± 4.3	10.34 ± 0.87	1.52 ± 0.1	201.7 ± 4.2
NGC 3949	6.51 ± 0.3	0.99 ± 0.03	164.5 ± 3.2	7.77 ± 0.41	1.12 ± 0.04	187.7 ± 2.5
NGC 3972	4.09 ± 0.23	1.18 ± 0.05	126.8 ± 2.9	4.4 ± 0.25	1.48 ± 0.06	162.9 ± 2.3
NGC 4062	2.98 ± 0.17	0.43 ± 0.02	149.4 ± 3.4	4.07 ± 0.27	0.53 ± 0.03	159.7 ± 2.7
NGC 4085	5.11 ± 0.54	1.12 ± 0.07	142 ± 6.1	5.84 ± 0.89	1.34 ± 0.13	174.8 ± 6.7
NGC 4096	1.07 ± 0.07	0.24 ± 0.01	110.1 ± 2.8	1.21 ± 0.09	0.26 ± 0.01	117.9 ± 2.1
NGC 4389	4.4 ± 1.02	1.56 ± 0.18	113.9 ± 10.6	6.45 ± 1.7	2.45 ± 0.28	179.2 ± 11.8
NGC 4569	6.23 ± 0.51	0.39 ± 0.03	205 ± 7	11.72 ± 1.18	0.67 ± 0.06	208.1 ± 5.2
NGC 5585	1.17 ± 0.07	0.94 ± 0.04	85.7 ± 1.8	0.9 ± 0.06	1.3 ± 0.08	109.6 ± 1.9
UGC 2259	0.77 ± 0.02	0.48 ± 0.01	88.8 ± 1	0.55 ± 0.02	0.49 ± 0.02	96.7 ± 0.9
UGC 3691	2.83 ± 0.14	0.86 ± 0.03	123.5 ± 2.3	2.96 ± 0.17	1.03 ± 0.04	147.5 ± 2.1
UGC 6399	1.34 ± 0.08	1.05 ± 0.04	86.7 ± 2	1.08 ± 0.09	1.48 ± 0.08	114.8 ± 2.5
UGC 6446	0.83 ± 0.04	0.73 ± 0.04	85.1 ± 1.4	0.43 ± 0.02	0.9 ± 0.06	91.2 ± 1.3
UGC 6818	1.31 ± 0.53	1.5 ± 0.32	73.1 ± 10.8	1.37 ± 0.75	2.78 ± 0.68	121.7 ± 16.7
UGC 6917	2.06 ± 0.11	1.04 ± 0.05	102.1 ± 2.2	1.75 ± 0.11	1.3 ± 0.07	129.3 ± 2
UGC 6923	0.96 ± 0.17	0.74 ± 0.1	86.5 ± 5.6	0.69 ± 0.16	0.91 ± 0.15	102.5 ± 5.9
UGC 7089	0.86 ± 0.08	1.15 ± 0.07	71.1 ± 2.3	0.71 ± 0.08	1.98 ± 0.14	103.3 ± 2.9
LSB GALAXIES						
F563-1	2.26 ± 0.16	1.06 ± 0.07	110.4 ± 2.7	1.48 ± 0.15	1.24 ± 0.14	124.1 ± 3.1
F568-3	3.08 ± 0.41	1.58 ± 0.13	110.9 ± 5.2	2.09 ± 0.42	2.13 ± 0.25	135.2 ± 6.8
F571-8	5.46 ± 0.84	1.40 ± 0.14	141.2 ± 8.0	4.86 ± 0.73	1.69 ± 0.17	167.0 ± 6.3

Table 3—Continued

Galaxy	\longleftarrow	MSTG		\longrightarrow	\longleftarrow	MOND	
	M ($10^{10} M_{\odot}$)	r_c (kpc)	v_0 (km s^{-1})	M ($10^{10} M_{\odot}$)	r_c (kpc)	v_c (km s^{-1})	
(1)	(2)	(3)	(4)	(5)	(6)	(7)	
F583-1	1.56 ± 0.12	1.28 ± 0.06	93.2 ± 2.3	0.90 ± 0.06	1.81 ± 0.07	109.4 ± 1.9	
NGC 247	2.27 ± 0.17	1.11 ± 0.06	109.4 ± 2.8	1.46 ± 0.14	1.35 ± 0.10	123.7 ± 2.9	
NGC 598	1.78 ± 0.04	0.64 ± 0.01	110.9 ± 0.8	1.15 ± 0.02	0.60 ± 0.01	116.4 ± 0.5	
NGC 1003	1.64 ± 0.03	0.08 ± 0.00	121.5 ± 0.8	1.66 ± 0.03	0.08 ± 0.00	127.6 ± 0.6	
NGC 1417	16.60 ± 0.49	0.92 ± 0.02	238.2 ± 2.8	23.30 ± 0.84	1.15 ± 0.03	247.0 ± 2.2	
NGC 3495	4.16 ± 0.27	0.87 ± 0.04	142.1 ± 3.3	4.01 ± 0.28	0.95 ± 0.04	159.2 ± 2.7	
NGC 3672	14.86 ± 0.20	1.21 ± 0.01	215.2 ± 1.2	17.02 ± 0.25	1.32 ± 0.01	228.4 ± 0.8	
NGC 3917	6.25 ± 0.45	1.60 ± 0.09	142.8 ± 3.8	5.18 ± 0.52	1.89 ± 0.15	169.7 ± 4.2	
NGC 4010	5.56 ± 0.88	1.62 ± 0.17	136.2 ± 7.9	4.66 ± 0.87	2.03 ± 0.24	165.2 ± 7.7	
NGC 4183	2.04 ± 0.11	0.85 ± 0.05	111.3 ± 2.0	1.35 ± 0.07	0.91 ± 0.06	121.2 ± 1.5	
UGC 6446	0.83 ± 0.04	0.73 ± 0.04	85.1 ± 1.4	0.43 ± 0.02	0.90 ± 0.06	91.2 ± 1.3	
UGC 6614	11.36 ± 1.79	1.24 ± 0.22	192.3 ± 11.9	9.90 ± 1.18	1.14 ± 0.16	199.5 ± 5.9	
UGC 6930	2.17 ± 0.13	1.03 ± 0.06	109.5 ± 2.2	1.40 ± 0.07	1.19 ± 0.07	122.2 ± 1.6	
UGC 6983	2.12 ± 0.16	0.90 ± 0.07	111.5 ± 2.8	1.34 ± 0.10	0.95 ± 0.09	121.0 ± 2.3	
HSB GALAXIES							
IC 342	7.95 ± 0.14	1.36 ± 0.03	188.3 ± 1.2	8.68 ± 0.16	1.44 ± 0.03	193.0 ± 0.9	
Milky Way	9.12 ± 0.28	1.04 ± 0.05	204.8 ± 2.4	10.60 ± 0.37	1.18 ± 0.05	202.9 ± 1.8	
NGC 224	20.19 ± 0.30	1.84 ± 0.04	259.6 ± 1.6	25.54 ± 0.45	2.17 ± 0.05	252.8 ± 1.1	
NGC 253	6.94 ± 0.25	0.86 ± 0.04	188.0 ± 2.5	7.88 ± 0.31	0.95 ± 0.04	188.4 ± 1.9	
NGC 300	2.03 ± 0.17	2.70 ± 0.19	101.7 ± 2.9	1.03 ± 0.09	2.93 ± 0.25	113.3 ± 2.5	
NGC 660	3.20 ± 0.06	0.54 ± 0.02	146.6 ± 0.9	2.99 ± 0.06	0.48 ± 0.02	147.8 ± 0.7	
NGC 801	20.07 ± 2.09	2.65 ± 0.24	240.3 ± 10.2	17.90 ± 2.05	2.44 ± 0.23	231.3 ± 6.6	
NGC 891	7.47 ± 0.17	0.78 ± 0.03	194.9 ± 1.7	8.49 ± 0.24	0.87 ± 0.04	192.0 ± 1.3	
NGC 1068	9.42 ± 0.54	1.11 ± 0.07	205.9 ± 4.5	12.96 ± 0.87	1.46 ± 0.09	213.4 ± 3.6	
NGC 1097	22.68 ± 0.31	1.19 ± 0.03	290.1 ± 1.6	29.64 ± 0.51	1.49 ± 0.04	262.4 ± 1.1	
NGC 1365	14.96 ± 0.25	1.29 ± 0.03	242.6 ± 1.6	18.51 ± 0.36	1.52 ± 0.04	233.2 ± 1.1	
NGC 1808	4.10 ± 0.10	0.51 ± 0.02	160.6 ± 1.4	4.32 ± 0.12	0.53 ± 0.02	162.1 ± 1.1	
NGC 2403	3.80 ± 0.13	2.09 ± 0.07	133.7 ± 1.6	2.77 ± 0.09	1.95 ± 0.07	145.1 ± 1.1	
NGC 2590	14.05 ± 0.48	1.10 ± 0.05	241.0 ± 3.3	17.54 ± 0.71	1.33 ± 0.07	230.1 ± 2.3	
NGC 2841	33.04 ± 1.31	2.19 ± 0.14	308.3 ± 5.2	41.07 ± 0.80	2.46 ± 0.07	284.7 ± 1.4	
NGC 2903	9.66 ± 0.61	1.72 ± 0.11	195.9 ± 4.8	10.61 ± 0.75	1.82 ± 0.12	202.9 ± 3.6	
NGC 2998	15.13 ± 1.20	2.52 ± 0.19	216.7 ± 6.8	14.05 ± 1.25	2.39 ± 0.19	217.7 ± 4.8	

Table 3—Continued

Galaxy	\longleftarrow	MSTG	\longrightarrow	\longleftarrow	MOND	\longrightarrow
	M ($10^{10} M_{\odot}$)	r_c (kpc)	v_0 (km s^{-1})	M ($10^{10} M_{\odot}$)	r_c (kpc)	v_c (km s^{-1})
(1)	(2)	(3)	(4)	(5)	(6)	(7)
NGC 3031	6.95 ± 0.12	0.67 ± 0.02	191.8 ± 1.3	7.97 ± 0.17	0.75 ± 0.02	188.9 ± 1.0
NGC 3034	0.52 ± 0.03	0.08 ± 0.01	85.0 ± 1.6	0.59 ± 0.05	0.09 ± 0.01	98.4 ± 2.0
NGC 3079	8.73 ± 0.23	0.77 ± 0.03	207.1 ± 2.1	10.42 ± 0.33	0.91 ± 0.04	202.0 ± 1.6
NGC 3198	5.55 ± 0.28	2.18 ± 0.12	152.1 ± 2.8	4.49 ± 0.26	2.05 ± 0.15	163.7 ± 2.4
NGC 3379	6.99 ± 0.06	0.45 ± 0.01	196.7 ± 0.6	8.13 ± 0.08	0.51 ± 0.01	189.9 ± 0.5
NGC 3379	6.99 ± 0.06	0.45 ± 0.01	196.7 ± 0.6	8.13 ± 0.08	0.51 ± 0.01	189.9 ± 0.5
NGC 3521	7.89 ± 0.10	0.80 ± 0.02	198.7 ± 1.0	9.12 ± 0.14	0.89 ± 0.02	195.4 ± 0.8
NGC 3628	9.13 ± 0.31	1.17 ± 0.05	202.3 ± 2.6	10.67 ± 0.41	1.32 ± 0.06	203.2 ± 2.0
NGC 3726	9.60 ± 1.37	4.07 ± 0.58	158.4 ± 8.8	7.22 ± 1.06	4.00 ± 0.72	184.3 ± 6.8
NGC 3769	2.59 ± 0.24	1.66 ± 0.20	121.7 ± 3.8	1.61 ± 0.16	1.34 ± 0.24	126.6 ± 3.2
NGC 3893	7.70 ± 1.00	1.74 ± 0.29	179.3 ± 8.9	7.85 ± 1.17	1.78 ± 0.34	188.2 ± 7.0
NGC 3953	20.47 ± 1.65	3.46 ± 0.28	225.5 ± 7.4	24.30 ± 1.94	3.92 ± 0.32	249.7 ± 5.0
NGC 3992	25.16 ± 2.32	2.77 ± 0.44	260.9 ± 10.0	28.35 ± 3.90	2.74 ± 0.72	259.5 ± 8.9
NGC 4013	6.01 ± 0.35	0.70 ± 0.19	181.1 ± 3.9	5.52 ± 0.26	0.16 ± 0.17	172.4 ± 2.1
NGC 4051	7.21 ± 1.31	2.58 ± 0.43	161.7 ± 11.1	6.20 ± 1.22	2.50 ± 0.47	177.4 ± 8.8
NGC 4088	9.74 ± 1.52	3.15 ± 0.51	172.4 ± 10.4	8.87 ± 1.46	3.23 ± 0.60	194.0 ± 8.0
NGC 4100	10.30 ± 1.59	2.89 ± 0.49	180.2 ± 10.8	9.91 ± 1.64	3.00 ± 0.58	199.5 ± 8.2
NGC 4138	4.31 ± 0.90	0.68 ± 0.39	160.7 ± 12.1	4.25 ± 1.03	0.62 ± 0.45	161.4 ± 9.8
NGC 4157	11.64 ± 1.21	2.92 ± 0.36	188.5 ± 7.7	11.05 ± 1.28	2.93 ± 0.43	205.0 ± 5.9
NGC 4217	12.92 ± 1.54	3.31 ± 0.36	189.7 ± 8.9	13.01 ± 1.66	3.49 ± 0.42	213.6 ± 6.8
NGC 4258	7.29 ± 0.14	0.84 ± 0.03	191.9 ± 1.4	7.79 ± 0.16	0.86 ± 0.03	187.8 ± 1.0
NGC 4303	3.08 ± 0.08	0.59 ± 0.02	143.8 ± 1.4	2.92 ± 0.08	0.55 ± 0.02	146.9 ± 1.0
NGC 4321	21.67 ± 0.45	2.12 ± 0.06	260.2 ± 2.2	28.20 ± 0.68	2.56 ± 0.07	259.1 ± 1.6
NGC 4448	1.98 ± 0.08	0.27 ± 0.01	127.8 ± 1.7	2.10 ± 0.09	0.28 ± 0.01	135.4 ± 1.4
NGC 4527	5.55 ± 0.23	0.79 ± 0.05	174.3 ± 2.7	6.02 ± 0.28	0.84 ± 0.05	176.2 ± 2.1
NGC 4565	18.11 ± 0.21	1.72 ± 0.03	251.2 ± 1.2	21.74 ± 0.32	1.93 ± 0.04	242.8 ± 0.9
NGC 4631	6.15 ± 0.10	1.34 ± 0.03	171.4 ± 1.0	6.36 ± 0.12	1.37 ± 0.03	178.6 ± 0.8
NGC 4736	3.15 ± 0.08	0.47 ± 0.02	146.8 ± 1.3	3.21 ± 0.09	0.47 ± 0.02	150.5 ± 1.1
NGC 4945	4.58 ± 0.12	0.63 ± 0.03	165.1 ± 1.6	4.65 ± 0.14	0.63 ± 0.03	165.1 ± 1.2
NGC 5033	9.90 ± 0.51	1.10 ± 0.08	210.2 ± 4.2	10.80 ± 0.70	1.15 ± 0.10	203.9 ± 3.3
NGC 5055	8.38 ± 0.06	1.11 ± 0.01	196.9 ± 0.5	8.44 ± 0.08	1.07 ± 0.02	191.6 ± 0.5
NGC 5194	7.29 ± 0.23	0.61 ± 0.03	196.6 ± 2.3	8.72 ± 0.30	0.71 ± 0.03	193.2 ± 1.7
NGC 5236	6.16 ± 0.12	1.10 ± 0.04	175.5 ± 1.3	5.56 ± 0.13	0.96 ± 0.04	172.6 ± 1.0
NGC 5457	10.20 ± 0.27	1.39 ± 0.04	206.5 ± 2.1	12.03 ± 0.36	1.57 ± 0.05	209.4 ± 1.6

Table 3—Continued

Galaxy	←	MSTG		→	←	MOND	
	M ($10^{10} M_{\odot}$)	r_c (kpc)	v_0 (km s^{-1})	M ($10^{10} M_{\odot}$)	r_c (kpc)	v_c (km s^{-1})	
(1)	(2)	(3)	(4)	(5)	(6)	(7)	
NGC 5533	28.81 ± 1.92	2.11 ± 0.23	293.2 ± 8.2	25.61 ± 1.68	1.68 ± 0.18	253.0 ± 4.1	
NGC 5907	4.59 ± 0.26	0.40 ± 0.05	169.3 ± 3.5	23.16 ± 0.46	2.35 ± 0.06	246.7 ± 1.2	
NGC 6503	1.98 ± 0.06	1.10 ± 0.05	117.4 ± 1.3	1.38 ± 0.05	0.91 ± 0.05	122.0 ± 1.0	
NGC 6674	32.48 ± 2.38	3.27 ± 0.33	277.7 ± 8.6	28.04 ± 2.43	2.70 ± 0.33	258.7 ± 5.6	
NGC 6946	8.95 ± 0.65	3.54 ± 0.27	161.2 ± 4.5	7.29 ± 0.61	3.57 ± 0.37	184.8 ± 3.8	
NGC 6951	6.22 ± 0.22	0.58 ± 0.03	185.8 ± 2.5	6.92 ± 0.28	0.63 ± 0.03	182.4 ± 1.9	
NGC 7331	21.47 ± 0.76	2.56 ± 0.10	248.9 ± 3.6	24.73 ± 0.83	2.74 ± 0.10	250.8 ± 2.1	
UGC 6973	6.41 ± 0.45	1.43 ± 0.12	172.5 ± 4.5	6.63 ± 0.46	1.46 ± 0.12	180.4 ± 3.1	

Note. — Best fit results according to both MSTG and MOND via a parametric mass distribution (independent of luminosity observations) — corresponding to the galaxy rotation curves of Figs. 2–4. Column (1) is the NGC/UGC galaxy number. The MSTG best fit results are presented in Columns (2) - (4), where Column (2) is the MSTG predicted total mass of the galaxy, M ; Column (3) is the MSTG predicted core radius, r_c ; and Column (4) is the predicted MSTG flat rotation velocity, v_0 , of equation (35). The MOND best results are presented in Columns (5) - (7), where Column (5) is the MOND predicted mass of the galaxy, M ; Column (6) is the MOND predicted core radius, r_c ; and Column (7) is the MOND asymptotic velocity, v_c of equation (31).

^aA MOND best fit was not possible due to $\langle M/L \rangle_{stars} < 0$. The MOND fit shown for DDO 154 neglects M_{disk} , whereas all the data was used for the MSTG result.

Table 4. OBSERVED & ACTUAL TULLY-FISHER RELATION RESULTS

	<i>B</i> -band	<i>K</i> -band	MSTG	MOND
	(1)	(2)	(3)	(4)
UMa Cluster of Galaxies — Photometric Fits				
<i>a</i>	2.67 ± 0.25	4.73 ± 0.44	3.19 ± 0.10	4.00 ± 0.10
<i>b</i>	-5.73 ± 0.54	-9.82 ± 0.95	-6.54 ± 0.21	-8.20 ± 0.01
<i>Complete Sample</i> of Galaxies — Parametric Fits				
<i>a</i>	2.89 ± 0.22	2.85 ± 0.33	2.68 ± 0.07	4.00 ± 0.00
<i>b</i>	-6.30 ± 0.47	-5.73 ± 0.74	-5.18 ± 0.16	-8.21 ± 0.00

Note. — The *B*-band luminosity data are taken from the original references except for Sofue (1996) and Romanowsky *et al.* (2003) which are taken from Tully (1988). The *K*-band luminosity data are taken from the 2MASS except for the Schombert F-type galaxies, which are taken from the original reference. The values of *a* and *b* are determined using a nonlinear least-squares fitting routine including estimated errors. Columns (1) and (2) are the best fit solutions to the observed Tully-Fisher relation, $\log(L) = a \log(v_{\text{out}}) + b$ in the *B*- and *K*-bands, respectively. Columns (3) and (4) are the best fit solutions to the actual Tully-Fisher relation, $\log(M) = a \log(v) + b$ for MSTG and MOND, where *v* is determined by equations (41) and (42), respectively. The observed & actual Tully-Fisher relation presented here are shown graphically in Figs. 6 & 7, respectively.